Cement and Concrete Research 142 (2021) 106373

Contents lists available at ScienceDirect

Cement and Concrete Research

journal homepage: www.elsevier.com/locate/cemconres

Deterioration mechanism of alkali-activated materials in sulfuric acid and the influence of Cu: A micro-to-nano structural, elemental and stable isotopic multi-proxy study

Cyrill Grengg [a,*], Gregor J.G. Gluth [b,*], Florian Mittermayr [c], Neven Ukrainczyk [d], Marko Bertmer [e], Ana Guilherme Buzanich [f], Martin Radtke [f], Albrecht Leis [g], Martin Dietzel [a]

[a] Institute of Applied Geosciences, Graz University of Technology, Rechbauerstraße 12, 8010 Graz, Austria
[b] Division 7.4 Technology of Construction Materials, Bundesanstalt für Materialforschung und -prüfung (BAM), Unter den Eichen 87, 12205 Berlin, Germany
[c] Institute of Technology and Testing of Building Materials, Graz University of Technology, Inffeldgasse 24, 8010 Graz, Austria
[d] Institute of Construction and Building Materials, Technical University of Darmstadt, Franziska-Braun-Strasse 3, 64 287, Darmstadt, Germany
[e] Felix Bloch Institute for Solid State Physics, Leipzig University, Linnéstraße 5, 04103 Leipzig, Germany
[f] Division 6.3 Structure Analysis, Bundesanstalt für Materialforschung und -prüfung (BAM), Richard-Willstätter-Straße 11, 12489 Berlin, Germany
[g] JR-AquaConSol GmbH, Joanneum Research, Steyrergasse 21, 8010 Graz, Austria

ARTICLE INFO

Keywords:
Durability
Alkali-activated cement
Corrosion
Microstructure
Modelling

ABSTRACT

In this study, a multi-proxy approach combining ^{29}Si, ^{27}Al and ^{1}H MAS-NMR, FEG-EPMA, XANES at the Cu K-edge and XRD analytics with hydrochemical tools such as ICP-OES analyses, oxygen-isotope signatures, and thermodynamic modelling was applied to K-silicate-activated metakaolin specimens - with and without $CuSO_4{\cdot}5H_2O$ addition - exposed to sulfuric acid at pH = 2 for 35 days. The results revealed a multistage deterioration mechanism governed by (i) acid diffusion, (ii) leaching of K-A-S-H, (iii) microstructural damage related to precipitation of expansive (K,Ca,Al)-sulfate-hydrate phases (iv) complete dissolution of the K-A-S-H framework, (v) and formation of silica gel in the outermost corroded regions. Copper ions were mainly located in layered spertiniite-chrysocolla-like phases in the as-cured materials. The results demonstrate an overall negative effect of Cu addition on chemical material durability, implying that the reported higher durability of Cu-doped AAM in biocorrosion environments can be best explained by bacteriostatic effects.

1. Introduction

The durability of concrete infrastructure in water supply, sanitation and waste management is a major concern in the task to maintain social standards of modern societies [1]. In this regard, frequently reported insufficient material performances [2–8] are mainly assigned to (micro) biological processes, such as fermentation, dissimilatory sulfate reduction or methanogenesis, associated with the formation of acidic solutions [9–11]. Corresponding types of corrosion are termed as microbial induced acid corrosion (MIAC; also referred to a biogenic acid corrosion (BAC)) in sewers and wastewater treatment facilities, or biocorrosion due to organic acids within (bio-)waste and biogas facilities. Within such systems, material durability is not only controlled by its resistance against the penetration of acidic solutions, but often also by its bioreceptivity, controlling microorganisms–concrete interactions [12–14].

Low-calcium alkali-activated materials (low-Ca AAM), also termed as geopolymers in the literature, have been frequently reported to exhibit high acid resistance [15–23], especially compared to conventional Portland cement-based (PC) binders [6,24,25]. Low-Ca AAM are formed via the combination of aluminosilicates (e.g. fly ash, blast furnace slag or metakaolin) with alkaline solutions (e.g. alkali silicate solutions; also known as waterglass), resulting in a highly connected polymeric network of SiO_4 and AlO_4 tetrahedra, charge balanced by alkali cations (commonly K, Na) [26,27]. Thereby, they avoid the formation of acid dissolvable calcium silicate hydrates (C-S-H) and calcium hydroxide ($Ca(OH)_2$), being the main structural-forming phases in PC binders [28]. Accordingly, AAM represent a promising group of materials to be applied for novel constructions or repair materials in the above-mentioned environments. Various physical, chemical, and microstructural properties, such as porosity [16,24], alkali ion of

* Corresponding authors.
E-mail addresses: cyrill.grengg@tugraz.at (C. Grengg), gregor.gluth@bam.de (G.J.G. Gluth).

https://doi.org/10.1016/j.cemconres.2021.106373
Received 18 June 2020; Received in revised form 1 December 2020; Accepted 14 January 2021
Available online 30 January 2021

activators [16,22], type of aluminosilicate [26], or Ca content [17,29] are known to strongly influence material acid resistance. Current models describe the deterioration of AAM under acid attack to proceed in three steps: 1) ion diffusion of aqueous species through the connected pore spaces and replacement of the non-framework alkali cation by hydronium ion ($H_3O^+ \equiv H^+$). 2) Hydrolysis and dealumination of the polymeric framework due to ongoing acid penetration [16]. 3) Reoccupation of framework vacancies by silica insertion [30,31]. In contrast, more recent studies yielded results implying complete dissolution at least of parts of the AAM framework and subsequent precipitation of amorphous silica [22,24].

Besides physicochemical material parameters, the bioreceptivity of material surfaces plays a crucial role in many of the aforementioned environments, by controlling biofilm development, activity and corresponding biogenic acid production [14,32,33]. One approach in this context is the incorporation of antimicrobial agents, such as (heavy-) metal ions, into building materials [34]. In recent years, metal ions were successfully applied to reduce bacterial growth on PC surfaces in various applications [34–36]. Due to described nano-structural similarities to zeolites, low-Ca AAM are associated with high cation-exchange properties, potentially enabling their application as stable carriers of antimicrobial agents [37,38]. However, information about the effects of heavy metal addition on AAM microstructure and subsequent performance in (bio)corrosive environments are scarce [21,39]. In one study it has been argued that the incorporation of Cu^{2+} and Co^{2+} ions into combined metakaolin and slag-based AAMs improved material abiotic acid resistance due to lower open porosities and reduced leaching pattern, when exposed to sulfuric acid [21]. The authors of that study further proposed a significantly higher complexity for AAM acid degradation mechanisms than previously reported in the literature.

The aim of the present study is to contribute to the above discussion by introducing a multi-proxy approach combining solid-state characterization by ^{29}Si, ^{27}Al and ^{1}H magic-angle spinning nuclear magnetic resonance (MAS NMR) spectroscopy, field-emission gun electron probe microanalyses (FEG-EPMA), X-ray absorption near-edge structure (XANES) spectroscopy at the Cu *K*-edge and X-ray diffraction (XRD) analyses with liquid characterization tools such as inductively coupled plasma optical emission spectrometry (ICP-OES) analyses, stable isotope distribution, and thermodynamic modelling. Therefore, exposure tests in diluted sulfuric acid (H_2SO_4) at pH = 2 over a period of 5 weeks were carried out for low-Ca metakaolin-based AAM, which were prepared with and without $CuSO_4{\cdot}5H_2O$. Focus was laid on the detailed material dissolution behavior of AAM when exposed to acidic environments, combined with the aim of understanding the impact of Cu^{2+} addition on the initial AAM composition and nano/microstructure, as well as its behavior when exposed to H_2SO_4. This purely abiotic approach was chosen in order to assess the effect of Cu^{2+} in AAM from an inorganic point of view, and to isolate chemical from bacteriostatic effects of Cu^{2+} ion addition when exposed to bio-corrosive environments.

2. Materials and methods

2.1. Starting materials and sample production

The chemical composition of the raw materials is given in Table 1. The potassium silicate solution (waterglass) had a solid content of 45 wt %, a molar ratio for SiO_2/K_2O of 1.5, pH of 13.5, and viscosity of 20 mPa s. Low-Ca AAM pastes were produced using a calcined clay powder, rich in metakaolin and quartz. Quantitative mineralogical characterization of the clay powder by XRD using Rietveld refinement (10 wt% spiked corundum) is given in Fig. S1, determining an amorphous (~metakaolin) content of 46 wt%, 40 wt% of quartz and 10 wt% of muscovite/illite.

AAM mix proportions are given in Table 2. Addition of $CuSO_4{\cdot}5H_2O$ (specimens with addition denoted as Cu9 and Cu94 henceforth) was done directly before mixing the metakaolin with waterglass. The amount of Cu addition was based on preliminary work, demonstrating a higher resistance of the material against BAC with the addition of 0.5 to 5 wt% $CuSO_4{\cdot}5H_2O$ (data not shown). Cu concentrations chosen for this study were selected to represent the high and low end of this range; sample designations reflect the approximate mass of $CuSO_4{\cdot}5H_2O$ per 2500 g of AAM (see Table 2). AAM paste specimens were mixed and cast according to EN 196–1, but without using sand aggregates and molded in two different sizes. Chemical compositions of the pastes were calculated based on chemical composition of individual components, which were evaluated by X-ray fluorescence analysis (XRF) using a wavelength dispersive X-ray fluorescence spectrometer (PANalytical 2404). For the leaching study, AAM pastes were initially cast in 150 × 150 × 80 mm molds. All specimens were cured sealed (100% relative humidity) for 28 days at 20 °C. After curing, the specimens for the acid exposure study were obtained by cutting the cured square prisms (150 × 150 × 80 mm) using a diamond-tipped saw into dimensions 75 × 75 × 37 mm. The open porosity was obtained by the water absorption measurements using the 160 × 40 × 40 mm specimen, which were first dried at 50 °C until reaching a constant mass, and subsequently water saturated under vacuum conditions. The mass of the dry and saturated sample and the sample volume (Archimedes method) were measured on at least three replicates. Compression tests were done according to EN 1015–3 and −11 on specimen size of 160 × 40 × 40 mm.

2.2. Exposure test set-up

Acid exposure tests were carried out on the AAM samples using an automatic titration reactor set-up. Each AAM specimen was placed into an individual reaction vessel (volume 1000 ml) over a floating magnetic stir bar rotating at 150 rpm and was submerged in 500 ml diluted sulfuric acid (96% Suprapur®; Sigma-Aldrich) solution exhibiting a pH of 2. During the exposure period of 5 weeks (for Ref and Cu9), the pH of the solution was kept constant at 2.0 by the titration of a 3 M H_2SO_4 solution using a peristaltic pump. The faster deterioration of the Cu94 specimen

Table 2
Sample mix proportion of metakaolin (MK) and K-waterglass (WG) and material parameters including water/binder ratio (w/b), open porosity in %, Si/Al ratio atomic ratios and compressive strength (CS) in MPa and including standard deviation (SD) measured after 28 days.

Sample ID	MK g	WG g	$CuSO_4{\cdot}5H_2O$ g	Material parameter			
				w/b[a]	Si/Al[b]	Porosity %	CS ± SD MPa
Ref	2000	1500	–	0.31	1.88	29.9	46.1 ± 2.0
Cu9	2000	1500	9.47	0.31	1.88	28.0	51.2 ± 1.8
Cu94	2000	1500	94.7	0.31	1.88	35.1	39.1 ± 1.6

[a] Water/(powder + solids in the activator).
[b] Determined via EPMA analyses.

Table 1
Chemical composition of the raw materials in mass %.

Raw materials	SiO_2	Al_2O_3	CaO	Fe_2O_3	TiO_2	MgO	Na_2O	K_2O	H_2O
Metakaolin	66.2	21.3	2.5	4.1	1.0	0.5	0.1	0.5	
Waterglass	22.0							23.0	55.0

led to a break-off of a larger part of the deterioration layer, which led to a blockage of the magnetic stir bar after 28 days of exposure. Accordingly, the exposure of Cu94 ended after 28 days. Both, the initial submerging solution and the titration solution were produced using isotopically light water in respect to ^{18}O ($\delta^{18}O = -103‰$ relative to VSMOW; cf. Section 2.8). pH and amount of acid dosage was constantly monitored using a computer controlled titrator device (Schott; TitroLine alpha plus). Specific electric conductivity (EC) was externally measured for each sampling using a WTW Multi350i instrument, equipped with a TetraCon325 electrode. Liquid samples were extracted after 10 min, 1, 2, 4, 8, 16 h, 1, 2, 4 days and 1, 2, 3, 4, 5 weeks. At each sampling event, 5 ml of experimental solution were extracted using a syringe. Immediately after sampling, the solutions were filtered through a 0.45 μm cellulose acetate membrane. Subsequently, a sub-sample of one ml was extracted and diluted with MQ water (omega = 18.2) for ICP-OES analyses. The remaining solutions were sealed and stored at 5 °C in a refrigerator for isotope analyses. A detailed illustration of the experimental set-up is shown in Fig. 1.

After the experiments, the specimens were photographed and dried at 40 °C for 48 h. Subsequently, they were stabilized in a layer of low viscosity epoxy resin (EpoThin; Buehler). After hardening of the resin, two cross sections of 5 mm thickness were cut from the middle of each specimen along the longitudinal axes, using a diamond saw. From one cross-section, slices with the dimensions of roughly 20 × 5 × 5 mm were cut from the surface near strongly deteriorated areas (henceforth labeled as Ref_corroded, Cu9_corroded and Cu94_corroded) and the interior intact matrix (henceforth labeled as Ref_intact, Cu9_intact and Cu94_intact) (for details see supplementary Fig. S2). Extracted slices were manually ground with mortar and pestle (agate) and the sample powders subsequently stored in closed glass vials in a desiccator at room temperature until required for XRD, XANES, and NMR analyses.

2.3. FEG-EPMA analyses

The second cross-section was embedded a second time in epoxy resin under vacuum conditions in order to guarantee the abrasion-free continuative preparation of the strongly deteriorated specimen (for detail see Fig. S2). The stabilized samples were polished, carbon coated and then analyzed with an electron probe Microanalyser (EPMA) using a JEOL JXA8530F Plus Hyper Probe (JEOL, Tokyo, Japan), equipped with a field-emission gun (FEG). Three types of measurements were recorded using the wavelength-dispersive analytical mode:

(i) (Semi)-quantitative element distribution images of Al, Ca, Cu, K, Si, S and Fe. The quantification of the individual element mappings in wt% were performed against mineral standards (microcline for Al, K and Si; augite for Ca; ilmenite for Fe; copper sulfide (CuS) for S and Cu). Elemental mappings were recorded at 15 kV and 30 nA, with a dwell time of 15 ms and a step size of either 3 μm (overview maps) or 1 μm (detail maps).

(ii) Quantitative spot measurements of Al, Ca, Cu, Si, S, Mg, Na, K and Fe were performed evenly distributed within the intact matrix, the transition zone, the deterioration layers, vein fillings and Cu grains of the different samples. Quantifications were performed against mineral standards. Microcline was used for Al, K, Si; augite for Ca and Mg; CuS for S and Cu; and ilmenite for Fe. Measurements were conducted for 20 s on the peak and 10 s on each background at 15 kV, 5 nA and a defocused beam with a diameter of ~1 μm.

(iii) Phase distribution maps: Chemical compositional data obtained from the quantitative spot measurements and the elemental mapping were further processed in space-resolved phase calculations using the XMapTool plugin application (version 3.3.1) in Matlab computer code (MathWorks, version 9.2.0 R2017a) [40]. In a first step the individual phases were manually quantified based on single spot analysis (see Fig. S4). Secondly theses phases were allocated to the corresponding X/Y-coordinates on the areas of elemental mappings and thirdly the phase distribution mapping was created by the software.

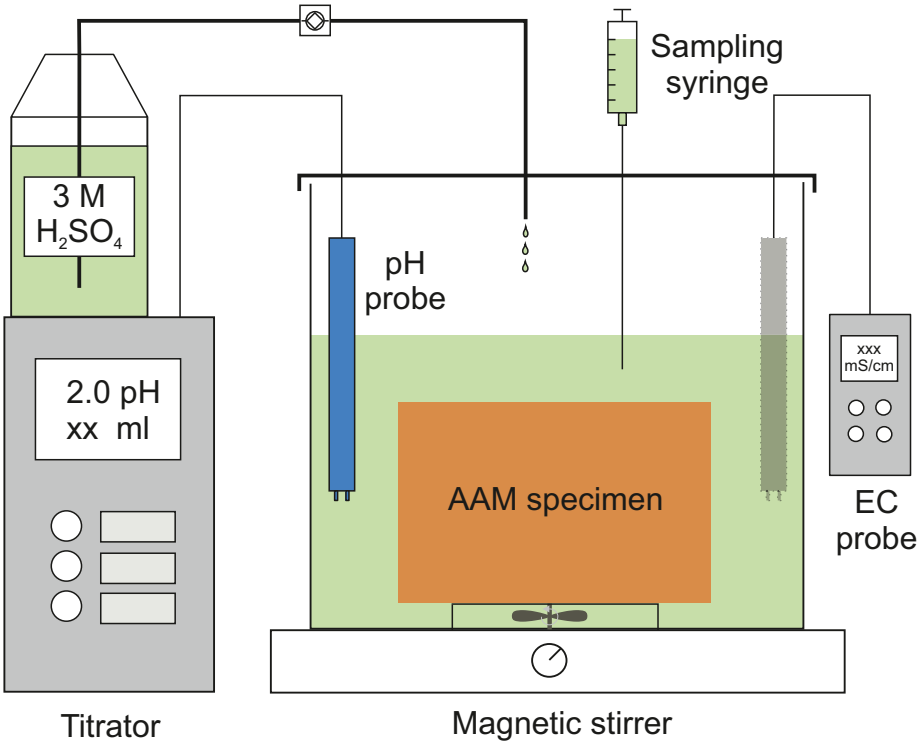

Fig. 1. Experimental set-up for the acid exposure experiments of the AAM specimens.

2.4. XRD measurements

Powders for X-ray diffraction (XRD) measurements were filled into sample holders by front loading. For samples from corroded layers of which only a small amount was available, flat sample holders had to be used, which led to transmission of radiation through the sample powder bed and diffraction from the sample holder. XRD patterns were recorded in Bragg–Brentano geometry on a Rigaku Ultima IV device under the following conditions: CuKα radiation ($\lambda = 1.541867$ Å); tube operating at 40 kV, 40 mA; sampling interval: 0.02° 2θ; scan rate: 0.5° 2θ min^{-1}; scanning range: 5°–65° 2θ; incident divergence slit (fixed): in-plane 0.5°, axial 10 mm; strip detector D/teX Ultra with 5° Soller slits. The sample holders were spun at 15 rpm during the measurements.

2.5. XANES measurements

X-ray absorption near-edge structure (XANES) spectroscopy measurements at the Cu *K*-edge were carried out at the BAM*line* at BESSY II [41] in fluorescence mode. The X-ray beam was monochromatized using a double crystal monochromator (DCM) in a Si(111) arrangement with an energy resolution of $\Delta E/E = 2 \times 10^{-4}$, corresponding to an energy resolution of about 1.7 eV at the Cu *K*-edge. The size of the beam was 4 mm × 2 mm. The powdered samples were fixed in the sample holders with adhesive tape. The fluorescence radiation was detected by an SDD detector (Bruker XFlash® 5030).

Photon energies were calibrated via measurement of a copper foil, assigning a value of 8979 eV to the main edge jump of its spectrum. Spectra of the samples were recorded in the range 8845–9585 eV, with energy steps of 0.5 eV in the vicinity of the absorption edge (8950–9009 eV). The obtained XANES spectra were processed with the *ATHENA* software (version 1.2.12) [42]. The spectra of the reference compounds (see below) were corrected for self-absorption effects with the corresponding tool ('Fluo' algorithm) of *ATHENA*. The pre-edge normalization was performed until 60 eV below the absorption edge and the post-edge normalization from 85 eV above the edge (except for the anhydrous copper sulfate, for which the start of the post-edge range had to be assigned closer to the edge because of the limited extension of the spectrum); a quadratic polynomial was used to fit the post-edge range in all cases.

Synthetic copper(II) sulfate pentahydrate ($CuSO_4{\cdot}5H_2O$, p.a. Merck) and natural chrysocolla (Arizona, USA; ~$(Cu,Al)_2H_2Si_2O_5(OH)_4{\cdot}nH_2O$) were measured as reference compounds. Muscovite/illite was found by XRD as an impurity in the chrysocolla specimen, but the former mineral is not expected to contain a significant amount of Cu and, thus, influence the Cu *K*-edge XANES spectrum. In addition, Cu *K*-edge XANES spectra of azurite ($Cu_3(CO_3)_2(OH)_2$), tenorite (CuO), copper(II) hydroxide ($Cu(OH)_2$; spertiniite) and anhydrous copper sulfate ($CuSO_4$) were obtained from the databases of the University of Chicago [43] and the Hokkaido University [44]. All reference spectra are shown in the Electronic Supplementary Material (Fig. S5). The spectra from the databases were recorded in transmission mode, but it is assumed that the general features of the spectra do not differ much from what would be obtained under the present experimental conditions (cf. ref. [45]); thus, they can be employed for qualitative comparison with the measured spectra.

2.6. NMR spectroscopy

Solid-state magic-angle spinning nuclear magnetic resonance (MAS NMR) experiments were carried out on a Bruker AVANCE 750 spectrometer (magnetic field 17.6 T) at frequencies of 748.58 MHz, 195.06 MHz and 148.72 MHz for ^{1}H, ^{27}Al and ^{29}Si, respectively.

The ^{29}Si MAS NMR spectra were recorded at a spinning frequency of 7 kHz using a 4 mm probe. The 90° pulse length was 2.5 μs, and the SPINAL sequence [46] was used for proton decoupling. At least 1280 scans were accumulated per specimen, and the recycle delay was set to 2 s. A sample of Q_8M_8 was used as secondary reference with a shift of 11.9 ppm for the Si atom next to the methyl group. The $Q^n(m\mathrm{Al})$ nomenclature for SiO_4 tetrahedra will be used throughout this article, where n denotes number of oxygen-bridges to neighboring SiO_4 and AlO_4 tetrahedra, and $m \leq n$ denotes the number of AlO_4 of these tetrahedra; for $m = 0$, the expression in parentheses is omitted.

For the ^{27}Al MAS NMR spectra, a spinning frequency of 10 kHz and a 4 mm probe were used. The pulse length was 1 μs, corresponding to a pulse angle of less than 30°. At least 1000 scans were accumulated per specimen, and the recycle delay was set to 0.1 s. ^{27}Al chemical shifts were referenced to aluminum nitrate solution by using K-alum as a secondary reference at 0.7 ppm [47].

^{1}H MAS NMR spectra were recorded at a spinning frequency of 25 kHz using a 2.5 mm probe. The 90° pulse length was 1.4 μs, and typically 128 scans were accumulated per specimen, using a rotor-synchronized Hahn-echo sequence and a recycle delay of 5 s. Chemical shifts were referenced using a sample of PDMS as secondary reference (0.07 ppm with respect to TMS).

2.7. Solution analytics and thermodynamic modelling

Major, minor and trace elemental concentrations of filtered liquid samples were analyzed via inductively coupled plasma – optical emission spectrometry (ICP-OES; analytical error: < 5%), using a PerkinElmer Optima8300DV inductively coupled plasma optical emission spectrometer.

Hydrochemical modelling was carried out using PHREEQC software code (version 3.1.7.9213) together with its LLNL database [48] in order to calculate aqueous speciation, ion activities and saturation indices of relevant solid phases ($SI_{solid} = \log(IAP/K_{sp})$; IAP: ion activity product; K_{sp}: solubility constant).

2.8. Stable isotope measurements

The oxygen isotopic composition of the sampled experimental solutions in respect to H_2O was analyzed with a Finnigan DELTAplus mass spectrometer using the classic CO_2-H_2O equilibrium method [49]. The obtained $\delta^{18}O$ water values (± 0.05‰) are given relative to Vienna Standard Mean Ocean Water (VSMOW) in ‰ according to the expression:

$$\delta^{18}O_{solution} = {}^{18}O/\frac{{}^{16}O_{solution} - {}^{18}O/{}^{16}O_{standard}}{{}^{18}O/{}^{16}O_{standard}} * 1000$$

3. Results and discussion

3.1. Visual and physical material evolution

Prior to exposure the specimens showed relatively smooth, dense and homogeneous surfaces with no visual crack formation or similar signs of deterioration (Fig. 2). The specimen Cu94 exhibited numerous randomly distributed dark-green mineral inclusions, corresponding to the high concentrations of Cu minerals formed (for details see below), while only a few of such inclusions were observed on the Cu9 specimen. With the addition of low amounts of Cu a small decrease in open porosity from 29.9 vol% (Ref) to 28.0 vol% (Cu9) was measured, while the higher Cu addition for Cu94 specimen led to a strong increase in open porosity to 35.1 vol%. Correspondingly, Cu9 exhibited slightly higher compressive strength (CS) values of 51.2 MPa compared to the 46.1 MPa measured for the Ref specimen, whereas Cu94 showed a strongly reduced CS of 39.1 MPa (Table 2).

After acid exposure, all specimens showed a high degree of visual deterioration. The apparent overall intensity of corrosion increased slightly with the quantity of Cu addition. Besides intensive crack formation and spalling of surface layers, high amounts of various translucent minerals had precipitated on the surface of the specimens forming mineral-mats on the top of specimen's surfaces, as well as crack fillings.

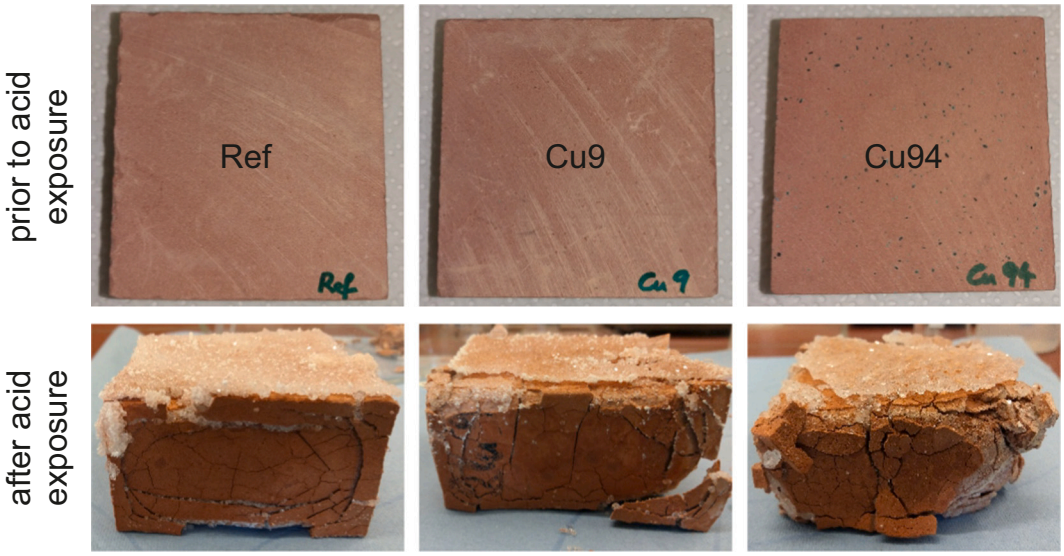

Fig. 2. Visual appearance of specimen before (top view) and after (side view) the exposure to H_2SO_4.

A detailed mineralogical characterization of these precipitates is given in Section 3.2.

3.2. Nano/microstructural analytics (FEG – EPMA, XRD, XANES, NMR)

FEG-EPMA spot analyses of the intact polymeric matrix showed little compositional or microstructural differences between the three different paste samples. The microstructural framework consisted mainly of amorphous potassium aluminosilicate phase (K-A-S-H = K_2O-Al_2O_3-SiO_2-H_2O) with an average chemical composition in wt% of 20.8 ± 0.7 Al_2O_3, 46.0 ± 0.3 SiO_2, 14.2 ± 0.4 K_2O, 1.5 ± 0.4 CaO and 3.0 ± 0.6 FeO (n = 168 single spot EPMA analyses), resulting in a total oxide mass of 86.4 ± 0.4 (Fig. 3B). The average molar Si/Al ratio of the polymeric matrix, calculated from this composition, is 1.88 (Table 2). Embedded in this framework lay randomly distributed unreacted quartz grains. The mass missing to give a total of 100 wt% corresponds mainly to analytical effects due to high micro- and nano-porosity of the material and partially to bound hydroxyls [50]. The impact of structural water might be of less importance here, since low-Ca AAM do not rely on hydroxyls as an integrally bound compound of the polymeric framework. Most of the present water is generally considered to be interstitial water within the pore structure of the matrix [25,51], where the charge-balancing alkali cations are bound into the network in hydrated form. A detailed summary of all measured spot analyses is given in the Tables S1 and S2.

BSE and elemental distribution images showed the transition between intact and corroded microstructure to be characterized by a sequence of elemental changes combined with micro- and macro-crack formation (Fig. 4). Within the inner transition zone with a thickness of few 100 μm, a slight decrease in K and Si and an increase in Al content was observed, together with the formation of a network of micro-cracks (~200 μm length), penetrating approximately perpendicular to the surface into the intact matrix (Fig. 4B). Interestingly, within the Cu94 specimen a Cu accumulation zone developed within this part of the transition zone (Fig. S3). The outer part of the transition zone is characterized by the formation of large, connected crack network systems, with a main parallel orientation in respect to the material surfaces. To a large extent these cracks are refilled with locally alternating sulfate mineral phases, clearly seen by high concentrations of Ca, S, K and Al (Fig. 4, Figs. S3 and S4). Based on compositional data these secondary precipitates were characterized as K-alum [$KAl(SO_4)_2{\cdot}12H_2O$], syngenite [$K_2Ca(SO_4)_2{\cdot}H_2O$], alunite [$KAl_3(SO_4)_2(OH)_6$], and anhydrite [$CaSO_4$] (potentially also bassanite [$CaSO_4{\cdot}0.5H_2O$] and gypsum [$CaSO_4{\cdot}2H_2O$]). This zone is further characterized by decreased Si and increased Al concentrations, compared to the intact region (Fig. 4).

The strongly corroded, surface-near layers were characterized by a disrupted and strongly cracked microstructure, exhibiting low Al and K (approx. 3.6–5.7 and 0.5–2.0 wt%, resp.) and high Si concentrations (Figs. 3C and 4, Tables S1 and S2). Considerably lower SiO_2 concentrations of 66 ± 5 wt% (n = 53) on average were measured within the samples containing Cu (Cu9 and Cu94) compared to the Ref specimen (71 ± 5 wt% (n = 19) wt%). At the same time, the average total oxide mass was 10 wt% lower in the Cu-containing specimens (74 wt% as compared to 84 wt% for Ref), indicating a higher porosity and higher H_2O content of the forming Si-gel layers in these materials.

Corresponding to the results obtained by FEG-EPMA analyses, no significant differences between the XRD patterns of the intact pastes were observed (Fig. 3A). All of them contained unreacted quartz, calcite, hematite and anatase as well as muscovite/illite (likely partially dehydroxylated) from the raw metakaolin precursor (Fig. S1). An "amorphous hump" centered at $d \approx 3.2$ Å (~28° 2θ) indicated amorphous alkali aluminosilicate phase (K-A-S-H in the present work) [52] as the major reaction product, produced via the alkali-activation of the metakaolin.

In the corroded layers of the pastes, K-alum, syngenite and alunite were identified in addition to the unreacted components of the metakaolin (Fig. 3A). This corresponds to the elemental distributions within the crack fillings, measured via FEG-EPMA analyses (Fig. 4). The phase assemblages observed by XRD differed slightly between the pastes with different Cu contents, with no K-alum found in specimen Cu94_corroded, and the presence of alunite in Ref_corroded and Cu9_corroded being uncertain. However, these differences were likely caused by the low abundance of these phases together with slight inhomogeneities of the corroded layers, as is indicated inter alia by the fact that K-alum was identified in Cu94_corroded via the NMR measurements (see below) and visually in large quantities as efflorescence on the specimen surface (see also Fig. 1). The distinct K-A-S-H amorphous hump was observed to shift its broad maximum from $d \approx 3.2$ Å (~28° 2θ) to $d \approx 4.0$ Å (~22° 2θ), indicating the dissolution of the initial K-A-S-H gel and the presence of an amorphous silica phase in these layers [22,25].

The overall Cu distribution within the intact matrix of the Cu9 and Cu94 specimen is mainly locally concentrated to grains with dimensions of up to several hundred microns. Two types of grains were identified, according to their size. The larger grains display a clear layered zonation, while the smaller ones are homogeneous (Fig. 5B & D). The core region of the layered grains consisted almost entirely of Cu with only a minor percentage of Si, corresponding to the chemical composition of

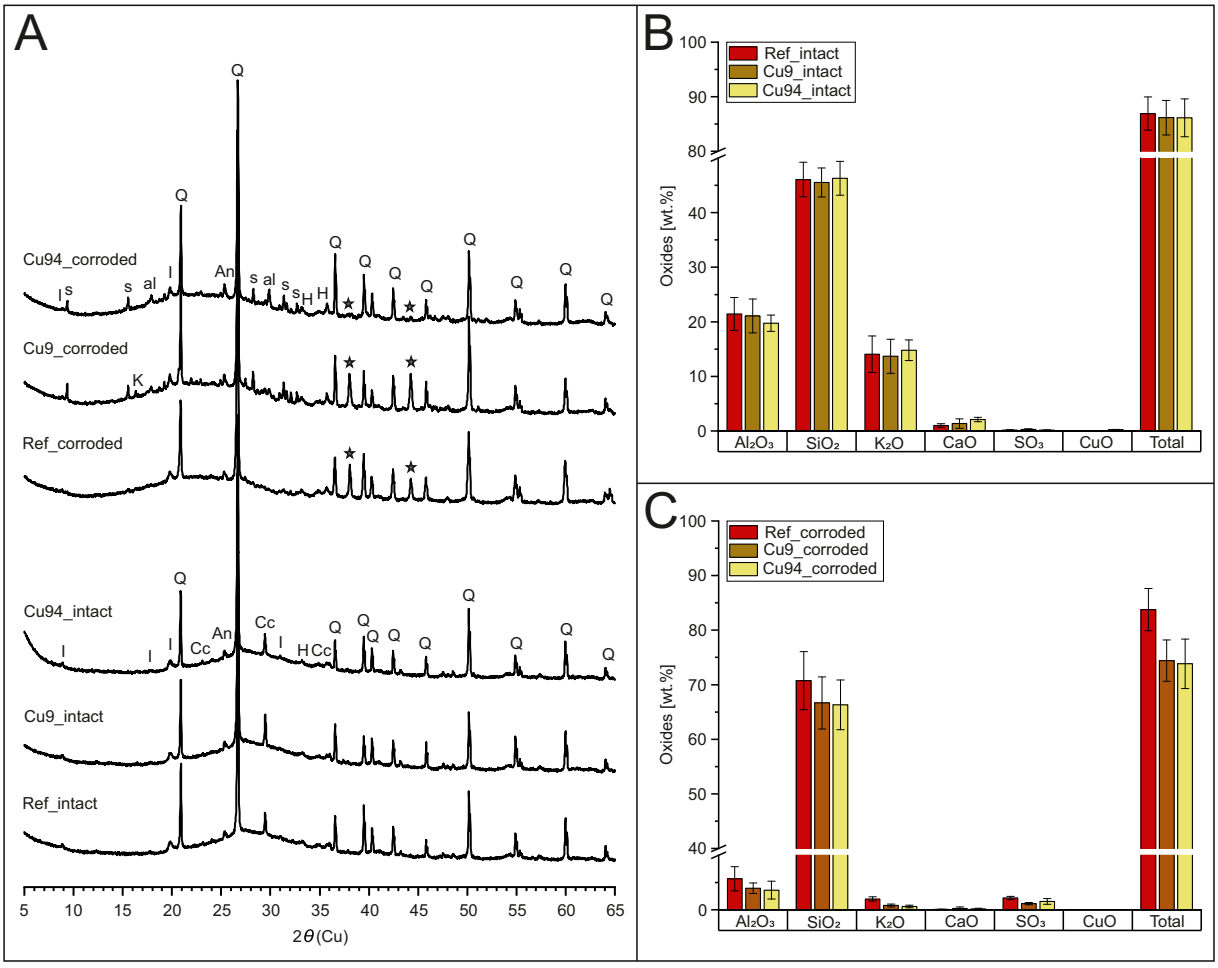

Fig. 3. (A) XRD patterns of samples from the intact and the corroded regions of the pastes. The ordinate is scaled as square root of intensity to enhance visibility of the smaller peaks. Major reflections are labeled: I, illite/muscovite; Q, quartz; Cc, calcite; An, anatase; H, hematite; s, syngenite; al, alunite; K, K-alum. Asterisks indicate reflections from the sample holder (Al). (B & C) Chemical composition presented as oxides of the AAM polymeric microstructure of the intact (B) and corroded (C) areas in wt%. $n = 168$ single spot analyses for intact and 72 for corroded, respectively.

spertiniite [$Cu(OH)_2$]. The average elemental concentrations of the inner rim zone correspond to the chemical composition of chrysocolla [$(Cu,Al)_2H_2Si_2O_5(OH)_4{\cdot}nH_2O$], while the outer rim zones and the smaller homogenous grains exhibit a chemical compositional mix between these two phases (Fig. 5C). Additionally, within the intact polymeric matrix of the Cu94 specimen low CuO concentrations of 0.3 ± 0.1 ($n = 31$) wt% were quantified, while Cu concentrations within the Cu9 specimen were below detection limit (<450 ppm). Within the inner transition zone between the intact and the corroded microstructure Cu concentrations increased to an average of 0.6 ± 0.2 ($n = 22$) and 0.3 ± 0.1 ($n = 21$) wt% in the Cu94 and Cu9 specimen, respectively (Fig. S3 and detailed in Tables S1 & S2). No Cu was detected within the strongly deteriorated microstructure.

The major features of the XANES spectra at the Cu *K*-edge of the measured paste samples are labeled A, B, C and D in Fig. 5A. Based on previous summaries [53,54], the first three of these can be assigned as follows: The pre-edge feature A at ~8978 eV corresponds to the Cu(II) 1 s → 3d electronic transition. This transition is forbidden in perfect octahedral oxygen coordination around Cu(II), and its intensity may thus be taken as an approximate measure of the average degree of distortion of CuO_6 octahedra. Feature B at ~8988 eV is assigned to the so-called Cu(II) 1 s → $4p_z$ + L → Cu(II) shakedown transition, and its separation from the main absorption peak reveals distortion of the CuO_6 octahedra from perfect symmetry as well. Feature C represents the Cu(II) 1 s → 4p electronic transition. In most Cu(II) compounds, copper is found in octahedral coordination, distorted to various degrees [55–57], thus potentially allowing differentiation of these compounds by the relative intensities and positions of the above features. The rare occurrence of 4- or 5-fold coordination of copper in some compounds [55], e.g. in azurite, can cause further changes of the Cu *K*-edge XANES spectrum, aiding identification.

The Cu *K*-edge XANES spectra of the samples from the intact paste samples Cu9_intact and Cu94_intact most closely resembled the spectrum of $Cu(OH)_2$ (Fig. 5A; all reference spectra shown in Fig. S5). The similarities include the comparatively low intensity of peak A, and the shapes and relative intensities of peaks B and C. Feature B was considerably less pronounced in the spectra of the intact regions than in the spectrum of tenorite (CuO). Importantly, the prominent feature D at approx. 9010–9020 eV distinguishes the spectra of the intact regions of the pastes from the spectra of $CuSO_4{\cdot}5H_2O$ and $CuSO_4$. It is noted that Farges et al. obtained almost identical Cu *K*-edge XANES spectra for several chrysocolla [$(Cu,Al)_2H_2Si_2O_5(OH)_4{\cdot}nH_2O$] specimens and spertiniite [$Cu(OH)_2$] [58].[1] Very similar Cu *K*-edge XANES spectra for chrysocolla and spertiniite were also reported by Takeda et al. [59]. In

[1] Based on these and other analyses, they concluded that chrysocolla is not a distinct mineral, but an intimate mixture of spertiniite and amorphous silica [58]. Contrary to that, more recent analytical results appear to confirm that chrysocolla is a mineral with structural features that differ from those of spertiniite [76,77].

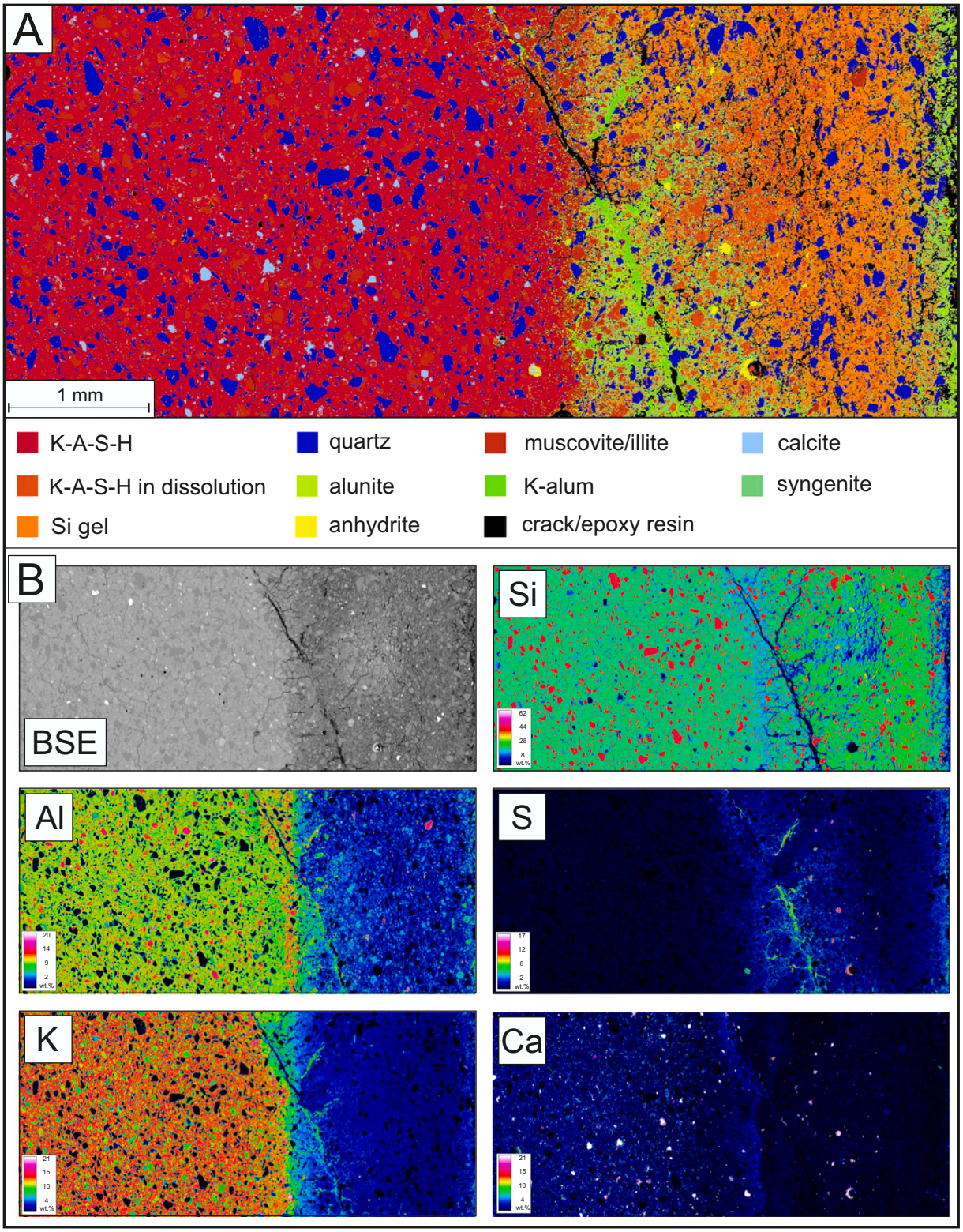

Fig. 4. (A) Mineral phase distribution image from the intact microstructure, the transition zone and the corrosion layer of the Cu9 specimen. (B) BSE image and elemental distribution images of Al, Si, S, K, Ca of the same area in wt%.

the present study, the spectra of $Cu(OH)_2$ and chrysocolla differed somewhat (Fig. S5), with the present spectrum of chrysocolla more similar to that obtained by McKeown [45] (viz. with a noticeable split of feature C into two features) than to the spectra reported by the other authors. However, the spectra of chrysocolla and spertiniite are generally too similar to enable differentiation of the corresponding phases in mixed spectra. This means that the spectra of the intact regions of the pastes were in accord with the presence of both $Cu(OH)_2$ and chrysocolla and, thus, support the results obtained via FEG-EPMA (Fig. 5B–D).

The XANES spectra of the corroded layers of both pastes were similar to each other and differed from the spectra of the intact regions; in particular, feature D at approx. 9010–9020 eV was much less

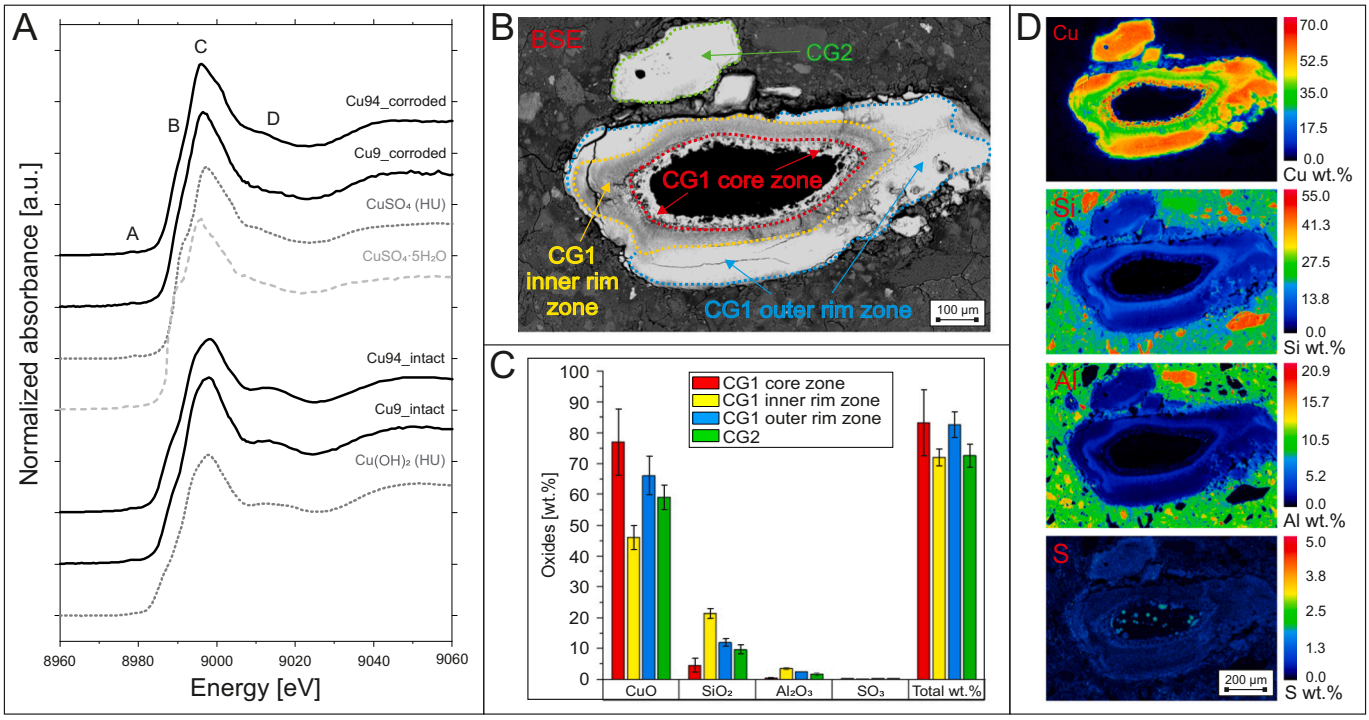

Fig. 5. (A) XANES spectra at the Cu K-edge of samples from the intact and the corroded regions of the Cu-containing pastes (full lines). For comparison, the spectra of copper(II) sulfate pentahydrate, anhydrous copper(II) sulfate and copper(II) hydroxide (grey, dotted or dashed lines; HU: Hokkaido University database) are shown. (B) BSE image of one layered Cu grain (CG1) and one small Cu grain showing homogeneous elemental distribution (CG2). (C) Average chemical compositions of the different zonation of the grains. (D) Element images of Cu, Si, Al and S of the Cu grains.

pronounced in the spectra of the corroded layers (Fig. 5A). Comparison with the available reference spectra (Fig. S5) yielded $CuSO_4$ and $CuSO_4{\cdot}5H_2O$ as the most likely copper phases in these layers.

The NMR spectra of the intact and corroded regions of pastes with and without the addition of Cu are shown in Fig. 6. The ^{29}Si MAS NMR spectra of the intact pastes were similar to each other, displaying mainly a broad hump centered at approx. −91 ppm (extending approximately from −74 ppm to −105 ppm) (Fig. 6A). Additionally, a minor resonance at −107 ppm in the spectrum of Cu94_intact, possibly also present in the spectrum of Ref_intact, was observed. The broad hump around −91 ppm

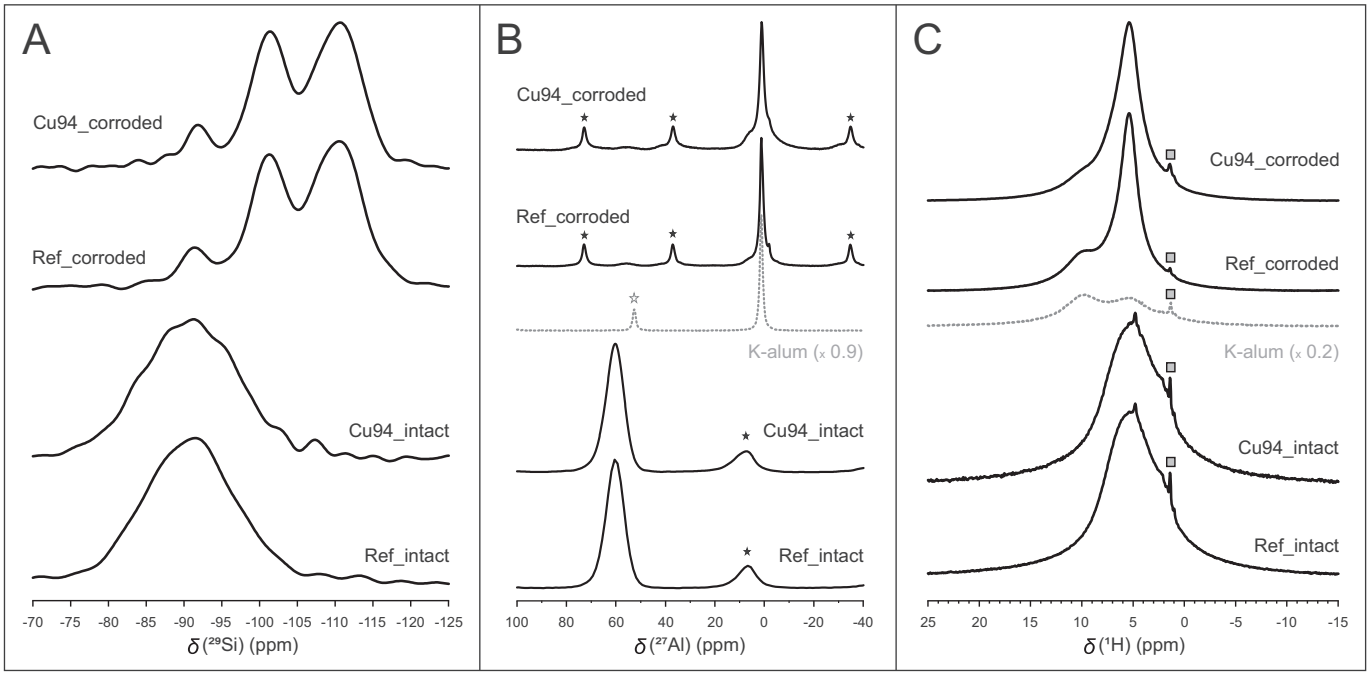

Fig. 6. MAS NMR spectra of the intact and corroded regions of Ref and Cu94 specimens. ^{29}Si MAS NMR spectra are displayed in (A). ^{27}Al MAS NMR spectra (full lines) together with the spectrum of K-alum (grey, dotted line) are shown in (B). Asterisks indicate spinning sidebands. (C) shows ^{1}H MAS NMR spectra of the specimens (full lines), and the spectrum of K-alum (grey, dotted line). Grey squares indicate an artifact resonance from the rotor cap material (polymer).

is in accordance with the presence of an amorphous K-A-S-H gel with a range of $Q^4(m\mathrm{Al})$ species [60–62]. The additional, minor resonance at −107 ppm can be assigned to Q^4 species in the quartz impurity [63] present in the metakaolin, in line with the mineralogical composition of the raw metakaolin precursor; however, the possibility that the apparent peak was due to noise in the spectrum cannot be excluded. The resonance at 60 ppm in the ^{27}Al MAS NMR spectra of the intact matrices is assigned to the 4-fold coordinated Al in the K-A-S-H gel [61,62,64]. The signal around 7 ppm in these spectra is a spinning sideband. It cannot be excluded that this signal overlapped a small resonance from 6-fold coordinated Al, for example in the illite/muscovite impurity of the metakaolin, but the abundance of this species would have been minor. The ^{1}H MAS NMR spectra of the intact regions of both pastes were dominated by a broad resonance centered at 5.1 ppm. This result is in line with previously reported ^{1}H MAS NMR spectra of AAM (N-A-S-H and K-A-S-H gels) [64,65]; the resonance is thus assigned to the water in the K-A-S-H gel. The small, narrow peak at 4.8 ppm on top of that resonance and the minor shoulder at about 2.2 ppm can be assigned to the small amounts of unreacted muscovite/illite in the materials [66].

In the ^{29}Si MAS NMR spectra of the samples from the corroded layers, the two dominating resonances were centered at approx. −101.5 ppm and − 110 ppm, respectively; both were relatively broad, indicating Si in an amorphous phase. Because Al in the corroded layers was primarily present in a crystalline phase (see below), the two resonances can be assigned to Q^3 and Q^4 species, respectively [63]. Further, based on the similarity of the spectra of the corroded layers and that of silica gel [67],

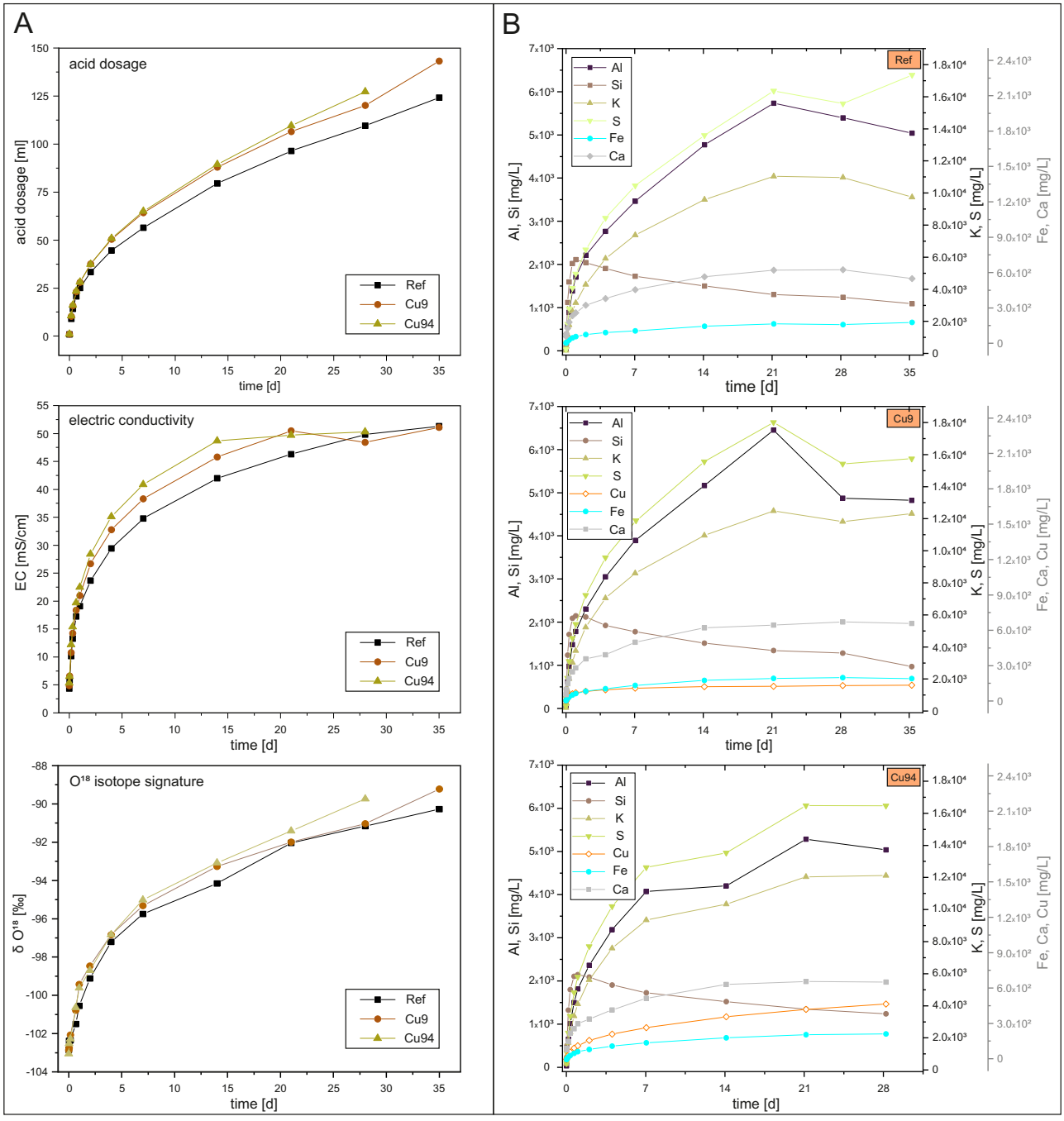

Fig. 7. Chemical evolution of the exposure solutions over time of Ref, Cu9 and Cu94 specimens. (A) Acid addition (ml), electric conductivity (EC; mS/cm) and evolution of ^{18}O isotopic signature (delta ^{18}O in ‰). (B) show elemental concentrations of dissolved species of Ref, Cu9 and Cu94.

it can be concluded that the major silica phase in the corroded layers was a silica gel. Analogous to previous observations [22], a small resonance at approx. −91.5 ppm was present in the ^{29}Si MAS NMR spectra of the corroded layers, which could be due to small amounts of altered K-A-S-H gel (i.e. $Q^4(m\mathrm{Al})$ species) that had remained in the corroded regions. The ^{27}Al MAS NMR spectra of the corroded regions of the pastes were dominated by a comparatively narrow resonance with its maximum at 1.1–1.3 ppm (Fig. 6B), i.e. within the AlO_6-chemical shift range. This resonance is assigned to K-alum, as it was narrow and virtually identical to that of the K-alum measured in the present study (spectrum included in Fig. 6B). The ^{27}Al MAS NMR spectra of the corroded regions of the pastes differed slightly in that the small, broader resonances at approx. 6 ppm and −2 ppm underlying the narrow resonance of K-alum had slightly higher relative intensities for the Cu-doped paste. The presence of these resonances proves that low amounts of an additional compound or compounds with AlO_6 were present in the specimens, but the resonances cannot be unequivocally assigned to a specific phase at this stage. The ^{1}H MAS NMR spectra of the corroded layers of both pastes exhibited two resonances with their maxima at 9.9 ppm and 5.4 ppm, respectively; the dominating resonance at 5.4 ppm was narrower than the signal from the K-A-S-H gel (Fig. 6C). Comparison with the measured spectrum of K-alum (included in Fig. 6C) shows that the resonance at 9.9 ppm can be fully assigned to the K-alum, while the signal at 5.4 ppm can be attributed to more than one phase: It is found in the spectrum of K-alum and could also originate from water and hydroxyls in another phase, e.g. the silica gel, which was the major phase in the corroded layers according to the above results.

3.3. Chemical solution evolution

The acid dosage and chemical evolution, including oxygen isotopic signatures, of the exposure solutions over time are displayed in Fig. 7. All three solutions exhibited an analog evolvement, resulting in similar absolute concentrations of dissolved species and corresponding electric conductivity (EC). However, due to variations in material degradation kinetics, variations between the absolute amount of acid addition and the rate of the increase of dissolved species were detected. In general, throughout the entire exposure time higher amounts of acid addition were observed for both Cu-containing specimens, resulting in roughly 10% higher total volume of dosage after 28 (for Cu94) and 35 days (for Cu9) compared to the Ref specimen (Fig. 7A). Correspondingly, a stronger incline in EC was observed for the Cu9 and Cu94 specimens reaching a plateau at roughly 50 ± 1.5 mS/cm after 14 (Cu94) and 21 (Cu9) days, respectively, whereas the Ref specimen reached similar EC values only after 28 days of exposure (Fig. 7A).

The evolution of dissolved species is characterized by two main trends (Fig. 7B): An initial period characterized by a rapid increase of the concentration of dissolved species, followed by a period in which the increase flattened and concentrations converged to a concentration plateau, or even decreased. Within this framework, dissolved species behavior can be subcategorized into 3 groups: (i) Si: shows a rapid increase in concentration within the first 24 h of exposure, followed by a continuous decrease, corresponding to the precipitation of amorphous Si gel phases (see below). (ii) Al, K, S: show a strong increase in concentration within the first 7, 14 and 21 days of exposure for Cu94, Cu9 and Ref, respectively, followed by constant or slightly decreasing concentrations. (iii) Ca, Fe and Cu (if present): exhibit a strong increase in concentration within the first 24 h, plateauing or nearly plateauing thereafter. The release of the elements grouped in (ii) and (iii) is expected to lead to secondary salt precipitation; the evolution of the saturation indices (SI_{solid}) of relevant minerals with time is displayed in Fig. 8B and will be discussed below. A complete summary of all thermodynamic modelling data is given in the supplementary materials Table S3.

Over the entire exposure period a strong enrichment of ^{18}O within the solvent solutions was observed (Fig. 7A). This can be seen from the strong increase in $\delta^{18}O$ from initially −102.9 ± 0.1‰ to −89 ± 0.5‰ after 5 weeks of exposure. This enrichment in ^{18}O vs ^{16}O is explained by oxygen isotope exchange between the bridging oxygens of the K-A-S-H framework tetrahedra (prepared with $\delta^{18}O_{water}$ = approx. −9‰, VSMOW) and the isotopically enriched acid solution ($\delta^{18}O_{water}$ = −103‰, VSMOW). In order to achieve this oxygen isotope exchange, the dissolution and corresponding breakdown of the tetrahedral structures of the AAM is required [68]. Accordingly, the observed isotopic trend directly reflects mainly the dissolution rates of the polymeric framework (together with the liberation of pore water from the AAM). In this regard, it is noted that the observed $\delta^{18}O$ increase of the experimental solution of more than 13‰ can only be achieved considering substantial dissolution rates. A system, in which the deterioration of the polymeric microstructure is solely controlled by dealumination and subsequent reoccupation of framework vacancies by silica, is unlikely to exhibit such strong isotopic exchange rates and associated isotope fractionation effects.

3.4. The mechanism of AAM deterioration in acid

As shown by the results presented above, the acid exposure of the AAM over the period of 5 weeks led to a complete transformation, in the

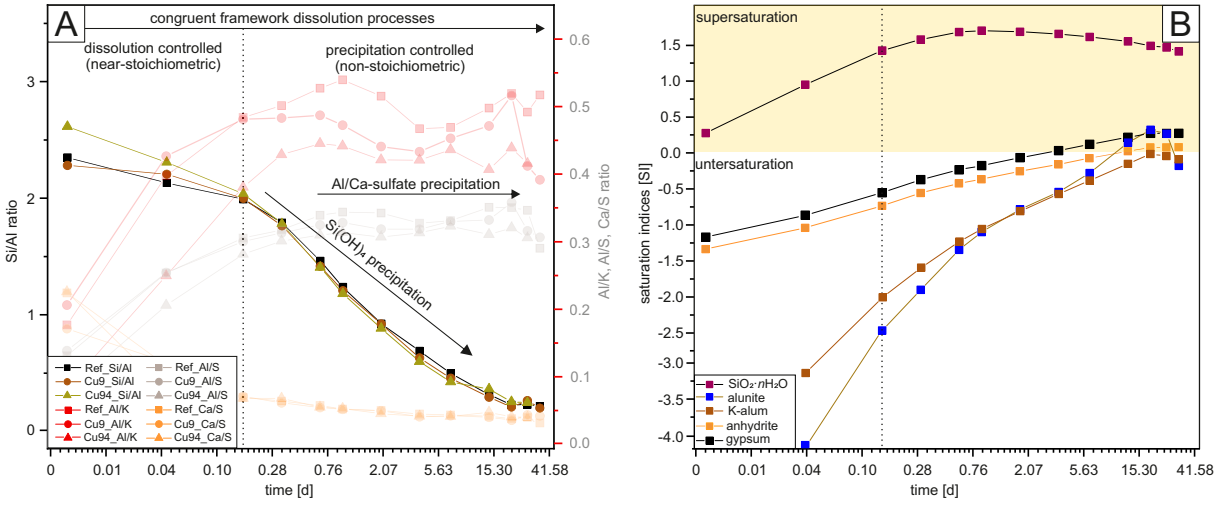

Fig. 8. Schematic description of relevant elemental ratios (Si/Al, Al/K, Al/S, Ca/S) (A) and saturation indices (SI) of relevant mineral phases (B) with time, indicating dissolution-controlled conditions within the first hours of exposure, followed by a precipitation-controlled regime.

corroded zone, of the highly connected K-A-S-H microstructure to a depleted Si gel-rich network. Basic considerations of the mechanisms of dissolution of zeolites [69,70] demonstrate that decomposition of a network aluminosilicate in acid will gradually shift from congruent Si and Al dissolution to a process that involves more and more leaching of Al, leaving behind amorphous silica-rich material, with progressing increase of Si/Al ratios; at Si/Al = 2, both processes occur simultaneously [69]. For the K-A-S-H gel of the cured AAM in the present study, which had an initial Si/Al ratio of 1.88 on average, it follows that dissolution caused by the acid attack involved the release of silicic acid species to a large extent, triggering subsequent precipitation as amorphous Si gel phase within the corrosion layers. In acidic conditions the dissolution of silica-containing solids are known to liberate monosilicic and polysilicic acids, where polymeric species are thermodynamically not stable, but at pH $\geq$ 2 their decomposition kinetics to monosilicic acid (depolymerization) is strongly retarded [71,72]. Moreover, dissolved Al ions strongly interact with silicic acids to form dissolved hydroxylalumosilicate (HAS) species/colloids - in particular valid for polysilicic species - which results in a further retardation of depolymerization of polymeric species to monosilicic acid (e.g. [73,74] and references therein). Accordingly, the precipitation of amorphous silica gel was still ongoing at the end of the experiment (Fig. 8), caused by the interplay of (i) the occurrence of long-lasting polysilicic acid and HAS in the solution and (ii) the slow precipitation kinetics of amorphous silica at low pH. Thus, it is concluded that the silica gel in the corroded layers of the AAM was principally formed by a through-solution process, in which the dissolution mechanisms and kinetics (rate of material dissolution) are dominated by the actual pH profile within the material.

An equivalent conclusion has been drawn previously for one-part AAM exposed to sulfuric acid and substantiated by $^{1}H—^{29}Si$ CP-MAS NMR spectra [22]. In contrast to that earlier study, the intact regions of the materials in the present study did not exhibit indications of Q^3 and Q^4 species (see NMR results), which proves that Si gel phases in the corroded layers are not simply unaltered remnants from the as-cured materials. This conclusion is strongly supported by the EPMA results, which show that Si accumulated in the corroded layer during acid attack, which would be difficult to explain without invoking the temporary existence of mobile Si species, i.e. Si in solution. A further indication of prevailing largely congruent material dissolution behavior is the strong enrichment of heavier ^{18}O isotopes within the experimental bulk solutions with reaction time, which strongly support the assumption of ongoing dissolution of Al and Si framework tetrahedra (Fig. 7A).

The overall deterioration kinetics of the materials can be subcategorized into a short initial, dissolution controlled phase, followed by a main diffusion–precipitation controlled period (Fig. 8A), due to the transition from far-from-equilibrium to close-to-equilibrium saturation conditions. In detail, within the first 4 to 8 h of exposure the dissolution of the K-A-S-H framework exhibits a near-stoichiometric behavior with Si/Al ratios in solution between 2.3 and 2.1 for materials Ref and Cu9. Initial higher Si/Al ratios of up to 2.6, measured immediately after acid exposure of Cu94, might be explained by the higher porosity of the material and associated faster release of monosilicic and polysilicic acids. Thereafter, due to the low solubility of amorphous silica at acidic conditions and the associated high supersaturation of amorphous silica ($SiO_2{\cdot}nH_2O$), the precipitation of Si gel is initiated, leading to decreasing Si/Al ratios in solution (Fig. 8A).

The continuous enrichment of K, Ca, Al and SO_4 in the solution due to leaching, dealumination and acid titration led to the precipitation of expansive sulfate salts, such as syngenite, alunite, K-alum and anhydrite (potentially also bassanite and gypsum) (Figs. 4, 9) within the strongly oversaturated pore solutions. Thermodynamic modelling indicates that precipitation occurred mainly within the last 3 weeks of exposure, where all of the described mineral phases are strongly supersaturated (Fig. 8B, Table S3). Described steady-state mineral precipitation is also reflected within the constant EC values during that period (Fig. 7a). However, it is likely that secondary mineral precipitation occurred even earlier within the pores of the transition horizon between intact and corroded microstructure, due to strong local environmental variability within the internal pore system, i.e. local supersaturation conditions. This dynamic, crack-inducing secondary mineral precipitation is primarily attributed to syngenite, alunite, K-alum and anhydrite as can be seen within the elemental composition of the crack-fillings (Fig. 4, Fig. S4, Fig. 9), representing a critical step regarding microstructural destabilization which increases diffusion rates of aqueous ions through

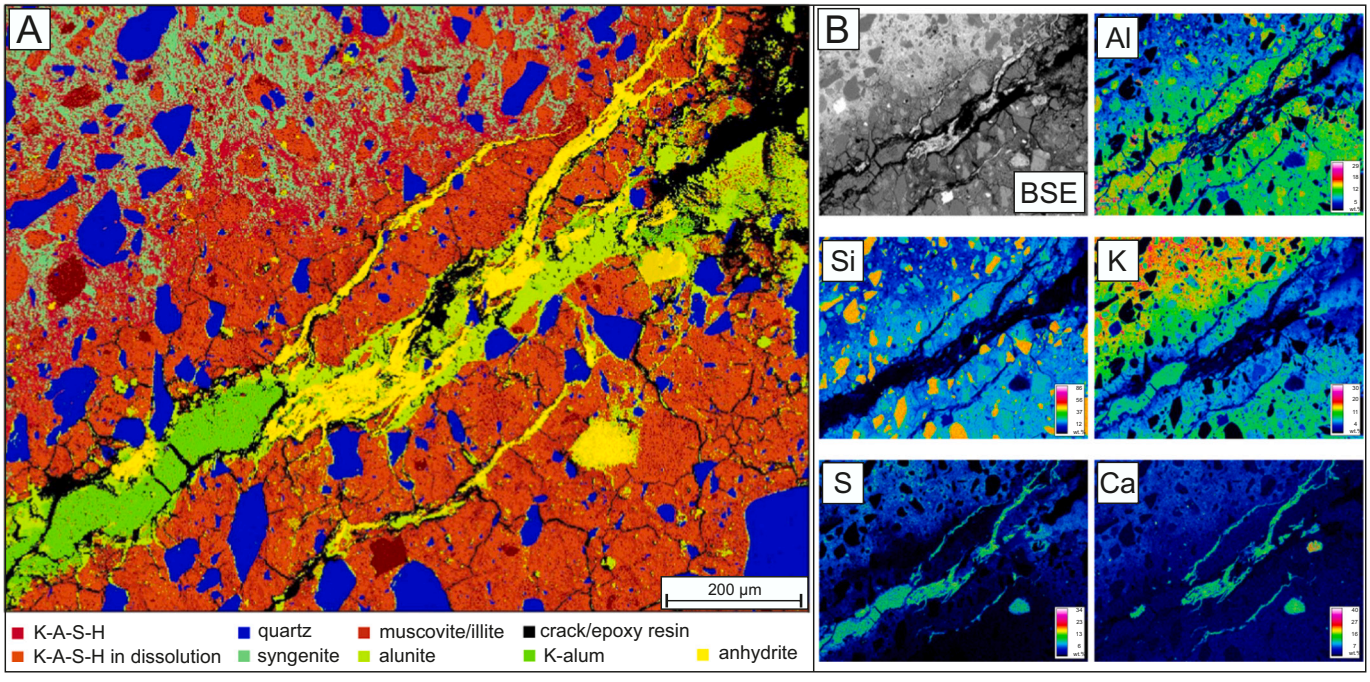

Fig. 9. (A) High-resolution mineral phase distribution image of the transition zone of the Cu9 specimen. (B) BSE image and elemental distribution images of Al, Si, S, K, Ca of the same area in wt%.

cracks. Within several areas syngenite precipitates dispersed within the inner transition zone, close to the intact K-A-S-H matrix, while K-alum, alunite and anhydrite constitute the main phases of the larger crack fillings (Fig. 9). This suggests a central role of syngenite regarding initial micro-crack formation within the material microstructure, which may be studied in more detail in future work.

Although the metakaolin-based AAM exhibit an average Ca concentration of only 1.1 ± 0.3 wt% within the initial material, it is concluded that precipitation of Ca sulfates was triggered by the accumulation of Ca and SO_4-rich pore solutions localized at the transition between intact and corroded material microstructure. Interestingly, beside syngenite, anhydrite (and bassanite) were found as the main Ca sulfate minerals present (Fig. S4). Reasons for this are presumably locally prevailing strongly oversaturated pore solutions and corresponding decreased water activity (a_{H2O}) [75].

Fig. 10 schematically summarizes the essential processes occurring during sulfuric acid attack on AAMs as demonstrated by the present results and the foregoing discussion.

3.5. *Effects of Cu on AAM microstructure and acid resistance*

One of the central aims of the current study was to understand the impact of Cu on the AAM microstructure and its chemical resistance against acid exposure. While hardly any differences between the chemical composition of the intact matrix of Cu-containing specimens (Cu9, Cu94) compared to the reference specimen without Cu addition (Ref) were observed, significant differences in porosity and compressive strength (CS) were detected. Probably because of that, increasing amounts of Cu addition resulted in higher corrosion rates as judged by visual inspection (Fig. 2). In this regard, the manner of Cu addition seems to play an important role. In the present study, Cu was added prior to the mixing as a $CuSO_4{\cdot}5H_2O$ powder to the metakaolin. Prevailing highly alkaline conditions during activation triggered immediate dissolution and re-precipitation in a grain-shaped manner, limiting Cu mobility and associated incorporation within the polymeric framework (see EPMA and XANES results). The observed chemical zonation within the grains corresponds to advancing polycondensation and ordering of the AAM framework during hardening and associated reducing Si availability. This is shown by the decreasing Si (and to a certain extent Al) concentrations within the outer layers of the grains, compared to the core zones, exhibiting the stoichiometry of chrysocolla. Cu incorporation was below the detection limit of ~450 ppm in the polymeric framework of the Cu9 specimen, while low average concentrations of 0.3 ± 0.1 wt% were measured in the Cu94 specimen. Based on the

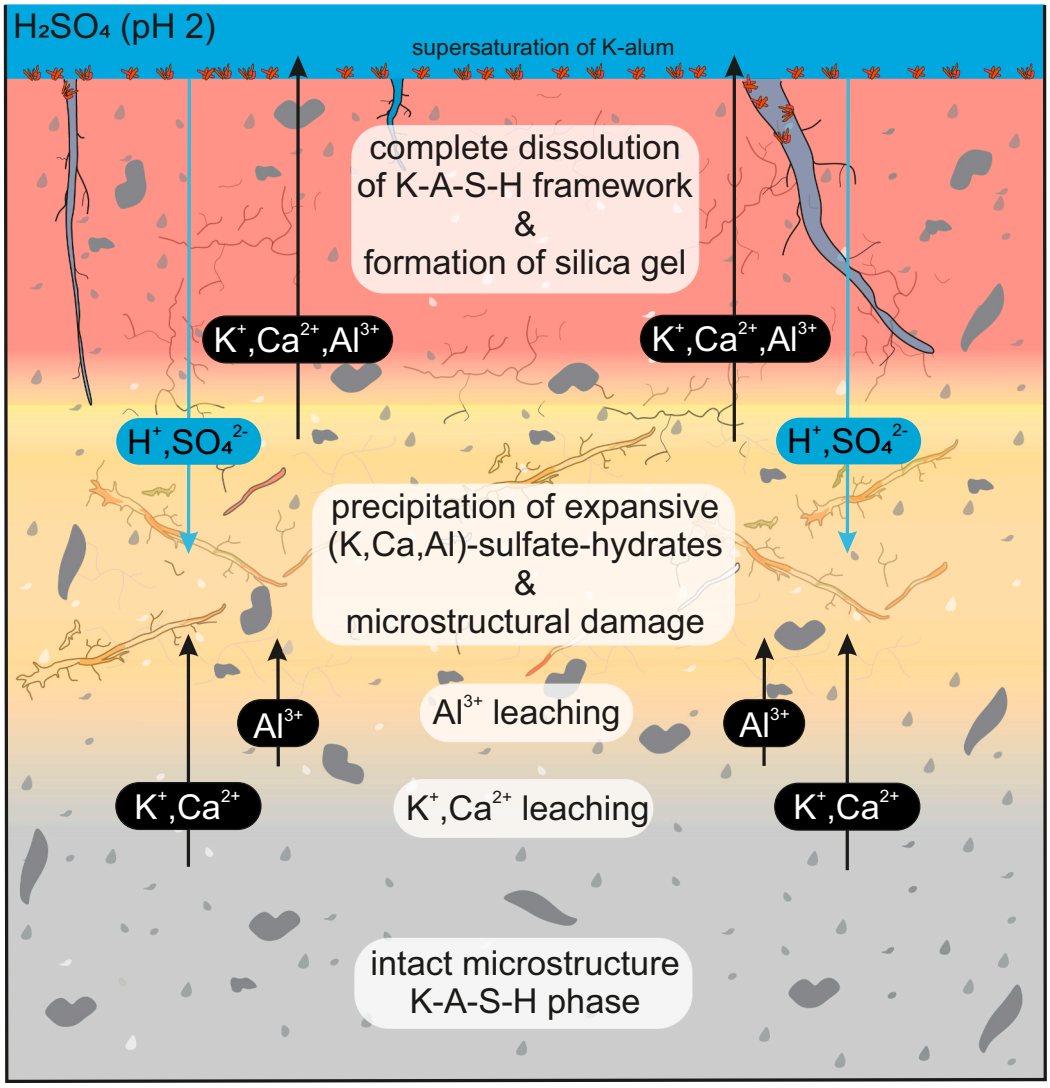

Fig. 10. Summary of the essential processes occurring during sulfuric acid attack on AAMs: (i) acid diffusion into the material, (ii) leaching of K^+, Ca^{2+} and Al^{3+} out of the K-A-S-H phase, (iii) precipitation of expansive (K,Ca,Al)-sulfate-hydrates and related microstructural damage, and (iv) complete dissolution of K-A-S-H framework and formation of silica gel.

results obtained in this study, ongoing preliminary experiments conducted by the authors (data not shown) demonstrated that a homogeneous Cu distribution could be achieved if Cu is pre-dissolved in H_2O and sprayed into the mixer with the liquid paste. The above aspects imply that higher corrosion intensities within the Cu-containing specimens are mainly caused by changes of physical material properties rather than changes of the chemical composition or nanostructure of the K-A-S-H gel phases. In addition, significantly lower Si concentrations and total amount of measured oxide masses were observed by EPMA within the amorphous Si gel phases of the corroded layers of the Cu-containing species (Fig. 3C) indicating prevailing higher porosities and water content. This increased porosity strongly reduced the protective effects of the Si gel against acid penetration [24], resulting in overall increased material dissolution rates, as demonstrated by the up to 10% higher total amount of acid titration (Fig. 7A). These conclusions are further supported by the ^{18}O isotope signatures showing a higher enrichment in ^{18}O vs ^{16}O for the Cu containing samples (Fig. 7A), which directly corresponds to the amount of oxygen liberated during the dissolution of the polymeric microstructure. Increased material dissolution rates (see also EC increase in Fig. 7A) in turn enhanced the precipitation rates and quantities of expansive secondary corrosion products, extending corresponding crack formation. Thus, it can be concluded that besides chemical properties of the attacking solution, also the precipitation kinetics have an impact on the mesostructure of the corrosion products, which in turn control further acid diffusion rates. The described trend increased with higher Cu addition, with similar amounts of dissolved species observed for the Cu94 specimen after only 15 days as for Cu9 after 20 days of exposure. The proposed higher dissolution rates are further supported by approximately 1.2‰ higher levels of ^{18}O enrichment for the Cu containing specimen (Fig. 7A).

The Cu present in the geopolymer matrix and the Cu-rich grains of Cu9 and Cu94 was partially released into solution on acid attack (cf. Fig. 7B), however at least some of it remained in the corroded layers in a $CuSO_4$- or $CuSO_4{\cdot}5H_2O$-like environment, as shown by the XANES spectra at the Cu *K*-edge (Fig. 5A). Whether $CuSO_4$ or $CuSO_4{\cdot}5H_2O$ domains actually existed in the corroded layers or the Cu was co-precipitated within other sulfates cannot be decided from the present results. In any case, copper is present in these layers in detectable amounts and may participate in subsequent reactions.

4. Conclusions

In this study, the mechanism of degradation of AAM caused by acid exposure and the impact of Cu addition on AAM nano/microstructure and acid resistance have been examined by exposing materials to sulfuric acid at pH = 2 over the period of 5 weeks. The obtained data are based on advanced material analytics, which combined with hydrochemical and oxygen isotope data from the experimental solutions, provide highly relevant, novel aspects for assessing the complex AAM deterioration process. The following main conclusions can be drawn:

- Results revealed an almost complete dissolution of the K-A-S-H gel of AAM in the corroded regions and the subsequent formation of silica gel as the main compound of the corrosion layers.
- Dynamic, crack-inducing secondary mineral precipitation is primarily attributed to alunite, K-alum, syngenite and anhydrite and represents a critical step regarding microstructural destabilization and associated increase in acid diffusion rates.
- Despite the low Ca concentrations within the AAM, Ca sulfates (mainly anhydrite and syngenite) seem to play a central role regarding crack-formation and associated microstructural degradation.
- Cu in the as-cured materials was found to predominantly accumulate in grains as spertiniite and chrysocolla, randomly distributed within the AAM structure. Additionally, within the Cu94 specimen, containing higher Cu concentrations, low quantities of Cu (0.3 ± 0.1 wt %) were dispersed within the polymeric framework. The method of metal ion addition appears to be crucial for metal ion distribution and structural incorporation.
- Variations in acid resistance between the Cu-doped and reference AAM were mainly correlated to changes in physical material properties, triggering higher ion diffusion rates and associated higher material dissolution rates for the materials with Cu addition. The increased dissolution kinetics resulted in Si gel formation exhibiting higher porosities, thereby reducing potential protective attributes of the Si gel layers.

The observed overall negative effects of Cu addition on the chemical acid resistance are in apparent contrast to previous reports of improved resistance of Cu-doped geopolymers in microbial induced acid corrosion-affected environments. The most parsimonious explanation for this apparent contradiction is that the higher durability of Cu-doped AAM within biocorrosion environments is mainly caused by bacteriostatic effects of the copper. Future work should test this proposition by comparing Cu-doped and Cu-free specimens, paralleling those in the present study, after long-term exposure to sewer environments.

CRediT authorship contribution statement

Cyrill Grengg: Conceptualization, Methodology, Validation, Formal Analysis, Investigation, Data curation, Writing – Original Draft, Writing – Review & Editing, Visualization.

Gregor J.G. Gluth: Conceptualization, Methodology, Validation, Formal Analysis, Investigation, Data curation, Writing – Original Draft, Writing – Review & Editing, Visualization.

Florian Mittermayr: Conceptualization, Methodology, Validation, Formal Analysis, Writing – Review & Editing, Visualization.

Neven Ukrainczyk: Methodology, Investigation, Validation, Writing – Review & Editing.

Marko Bertmer: Methodology, Formal Analysis, Investigation, Writing – Review & editing.

Ana Guilherme Buzanich: Investigation, Writing – Review & Editing.

Martin Radtke: Investigation.

Albrecht Leis: Investigation, Writing – Review & Editing.

Martin Dietzel: Conceptualization, Formal Analysis, Investigation, Writing – Review & Editing.

Declaration of competing interest

The authors declare that they have no known competing financial interests or personal relationships that could have appeared to influence the work reported in this paper.

Acknowledgement

The authors gratefully thank Andrea Wolf for her assistance in the lab and the Helmholtz-Zentrum Berlin (HZB) for the allocation of synchrotron radiation beamtime.

Appendix A. Supplementary data

Supplementary data to this article can be found online at https://doi.org/10.1016/j.cemconres.2021.106373.

References

[1] T. Hvitved-Jacobsen, J. Vollertsen, A.H. Nielsen, Sewer Processes - Microbial and Chemical Process Engineering of Sewer Networks, 2nd ed., CRC Press, London, 2013.

[2] M.G.D. Gutiérrez-Padilla, A. Bielefeldt, S. Ovtchinnikov, M. Hernandez, J. Silverstein, Biogenic sulfuric acid attack on different types of commercially

produced concrete sewer pipes, Cem. Concr. Res. 40 (2010) 293–301, https://doi.org/10.1016/j.cemconres.2009.10.002.
[3] J. Herisson, E.D. van Hullebusch, M. Moletta-Denat, P. Taquet, T. Chaussadent, Toward an accelerated biodeterioration test to understand the behavior of Portland and calcium aluminate cementitious materials in sewer networks, Int. Biodeterior. Biodegradation 84 (2013) 236–243, https://doi.org/10.1016/j.ibiod.2012.03.007.
[4] M.W. Kiliswa, K.L. Scrivener, M.G. Alexander, The corrosion rate and microstructure of Portland cement and calcium aluminate cement-based concrete mixtures in outfall sewers: a comparative study, Cem. Concr. Res. 124 (2019), https://doi.org/10.1016/j.cemconres.2019.105818.
[5] B.R.L. Islander, J.S. Devinny, A. Member, F. Mansfeld, A. Postyn, H. Shih, Microbial ecology of crown corrosion in sewers, J. Environ. Eng. 117 (1991) 751–770.
[6] B. Drugă, N. Ukrainczyk, K. Weise, E. Koenders, S. Lackner, Interaction between wastewater microorganisms and geopolymer or cementitious materials: biofilm characterization and deterioration characteristics of mortars, Int. Biodeterior. Biodegrad. 134 (2018) 58–67, https://doi.org/10.1016/j.ibiod.2018.08.005.
[7] G. Jiang, M. Zhou, T.H. Chiu, X. Sun, J. Keller, P.L. Bond, Wastewater-enhanced microbial corrosion of concrete sewers, Environ. Sci. Technol. 50 (2016) 8084–8092, https://doi.org/10.1021/acs.est.6b02093.
[8] M. Valix, K. Shanmugarajah, Biogenic acids produced on epoxy linings installed in sewer crown and tidal zones, Water Res. 80 (2015) 217–226, https://doi.org/10.1016/j.watres.2015.05.027.
[9] H.S. Jensen, PhD Thesis; Hydrogen Sulfide Induced Concrete Corrosion Of Sewer Networks, Aalborg University, 2009.
[10] H.S. Jensen, P.N.L. Lens, J.L. Nielsen, K. Bester, A.H. Nielsen, T. Hvitved-Jacobsen, J. Vollertsen, Growth kinetics of hydrogen sulfide oxidizing bacteria in corroded concrete from sewers, J. Hazard. Mater. 189 (2011) 685–691, https://doi.org/10.1016/j.jhazmat.2011.03.005.
[11] A.H. Nielsen, J. Vollertsen, H.S. Jensen, H.I. Madsen, T. Hvitved-Jacobsen, Aerobic and anaerobic transformations of sulfide in a sewer system – field study and model simulations, Proc. Water Environ. Fed. 2006 (2006) 3654–3670, https://doi.org/10.2175/193864706783751447.
[12] M. Alexander, A. Bertron, N. De Belie, Performance of Cement-Based Materials in Aggressive Aqueous Environments, 1st ed., Springer, Ghent, 2013 https://doi.org/10.1007/978-94-007-5413-3.
[13] M. Peyre Lavigne, C. Lors, M. Valix, J. Herrison, E. Paul, A. Bertron, Microbial induced concrete deterioration in sewers environment: Mechanisms and microbial populations, Proc. Microorg. Mater. Interact. (2016) 1–17.
[14] A. Buvignier, M. Peyre-Lavigne, O. Robin, M. Bounouba, C. Patapy, A. Bertron, E. Paul, Influence of dissolved-aluminum concentration on sulfur-oxidizing bacterial activity in the biodeterioration of concrete, Appl. Environ. Microbiol. 85 (2019) 1–12, https://doi.org/10.1128/aem.00302-19.
[15] R.R. Lloyd, J.L. Provis, J.S.J. Van Deventer, Acid resistance of inorganic polymer binders. 1. Corrosion rate, Mater. Struct. 45 (2012) 1–14, https://doi.org/10.1617/s11527-011-9744-7.
[16] T. Bakharev, Resistance of geopolymer materials to acid attack, Cem. Concr. Res. 35 (2005) 658–670, https://doi.org/10.1016/j.cemconres.2004.06.005.
[17] P.S. Deb, P.K. Sarker, S. Barbhuiya, Sorptivity and acid resistance of ambient-cured geopolymer mortars containing nano-silica, Cem. Concr. Compos. 72 (2016) 235–245, https://doi.org/10.1016/j.cemconcomp.2016.06.017.
[18] C. Montes, E.N. Allouche, Evaluation of the potential of geopolymer mortar in the rehabilitation of buried infrastructure, Struct. Infrastruct. Eng. 8 (2012) 89–98, https://doi.org/10.1080/15732470903329314.
[19] V. Sata, A. Sathonsaowaphak, P. Chindaprasirt, Resistance of lignite bottom ash geopolymer mortar to sulfate and sulfuric acid attack, Cem. Concr. Compos. 34 (2012) 700–708, https://doi.org/10.1016/j.cemconcomp.2012.01.010.
[20] A. Fernandez-Jimenez, I. García-Lodeiro, A. Palomo, Durability of alkali-activated fly ash cementitious materials, J. Mater. Sci. 42 (2007) 3055–3065, https://doi.org/10.1007/s10853-006-0584-8.
[21] J.P. Gevaudan, A. Caicedo-Ramirez, M.T. Hernandez, W.V. Srubar, Copper and cobalt improve the acid resistance of alkali-activated cements, Cem. Concr. Res. 115 (2019) 327–338, https://doi.org/10.1016/j.cemconres.2018.08.002.
[22] P. Sturm, G.J.G. Gluth, C. Jäger, H.J.H. Brouwers, H.C. Kühne, Sulfuric acid resistance of one-part alkali-activated mortars, Cem. Concr. Res. 109 (2018) 54–63, https://doi.org/10.1016/j.cemconres.2018.04.009.
[23] H.A. Khan, M.S.H. Khan, A. Castel, J. Sunarho, Deterioration of alkali-activated mortars exposed to natural aggressive sewer environment, Constr. Build. Mater. 186 (2018) 577–597, https://doi.org/10.1016/j.conbuildmat.2018.07.137.
[24] C. Grengg, N. Ukrainczyk, G. Koraimann, B. Mueller, M. Dietzel, F. Mittermayr, Long-term in situ performance of geopolymer, calcium aluminate and Portland cement-based materials exposed to microbially induced acid corrosion, Cem. Concr. Res. 131 (2020), https://doi.org/10.1016/j.cemconres.2020.106034.
[25] N. Ukrainczyk, M. Muthu, O. Vogt, E. Koenders, Geopolymer, calcium aluminate, and portland cement-based mortars: comparing degradation using acetic acid, Materials (Basel) 12 (2019), https://doi.org/10.3390/ma12193115.
[26] J.L. Provis, J.S.J. van Deventer, Geopolymers. Structures, Processing, Properties and Industrial Applications, CRC Press, Cambridge, UK, 2009, https://doi.org/10.1533/9781845696382.
[27] P. Duxson, A. Fernández-Jiménez, J.L. Provis, G.C. Lukey, A. Palomo, J.S.J. Van Deventer, Geopolymer technology: the current state of the art, J. Mater. Sci. 42 (2007) 2917–2933, https://doi.org/10.1007/s10853-006-0637-z.
[28] C.L. Page, M.M. Page, Durability of Concrete and Cement Composites, CRC Press, 2007.
[29] J. Aliques-Granero, T.M. Tognonvi, A. Tagnit-Hamou, Durability test methods and their application to AAMs: case of sulfuric-acid resistance, Mater. Struct. 50 (2017) 1–14, https://doi.org/10.1617/s11527-016-0904-7.
[30] A. Allahverdi, F. Škvára, Nitric acid attack on hardened paste of geopolymeric cements, Ceramics-Silikáty 45 (2001) 143–149.
[31] A. Allahverdi, F. Škvára, Sulfuric acid attack on hardened paste of geopolymer cements Part 2. Corrosion mechanism at mild and relatively low concentrations, Ceramics-Silikáty 50 (2006) 1–4.
[32] A. Buvignier, C. Patapy, M.P. Lavigne, E. Paul, A. Bertron, Resistance to biodeterioration of aluminium-rich binders in sewer network environment: study of the possible bacteriostatic effect and role of phase reactivity, Cem. Concr. Res. 123 (2019) 105785, https://doi.org/10.1016/j.cemconres.2019.105785.
[33] C. Lors, E. Dorelle, H. Miokono, D. Damidot, Interactions between Halothiobacillus neapolitanus and mortars: comparison of the biodeterioration between Portland cement and calcium aluminate cement, Int. Biodeterior. Biodegradation 121 (2017) 19–25, https://doi.org/10.1016/j.ibiod.2017.03.010.
[34] C. Grengg, F. Mittermayr, N. Ukrainzcyk, G. Koraimann, S. Kienesberger, M. Dietzel, Advances in mineral based construction materials for sewer systems affected by microbiological induced concrete corrosion: a review, Water Res. 134 (2018) 341–352, https://doi.org/10.1016/j.watres.2018.01.043.
[35] A. Alum, A. Rashid, B. Mobasher, M. Abbaszadegan, Cement-based biocide coatings for controlling algal growth in water distribution canals, Cem. Concr. Compos. 30 (2008) 839–847, https://doi.org/10.1016/j.cemconcomp.2008.06.012.
[36] E. Vincke, N. Boon, W. Verstraete, Analysis of the microbial communities on corroded concrete sewer pipes - a case study, Appl. Microbiol. Biotechnol. 57 (2001) 776–785, https://doi.org/10.1007/s002530100826.
[37] S. Hashimoto, T. MacHino, H. Takeda, Y. Daiko, S. Honda, Y. Iwamoto, Antimicrobial activity of geopolymers ion-exchanged with copper ions, Ceram. Int. 41 (2015) 13788–13792, https://doi.org/10.1016/j.ceramint.2015.08.061.
[38] F. Pacheco-Torgal, J. Labrincha, C. Leonelli, A. Palomo, P. Chindaprasit, Handbook of Alkali- Activated Cements, Mortars and Concretes, 1st Editio, Woodhead Publishing, 2014, https://doi.org/10.1016/C2013-0-16511-7.
[39] B. Druga, K. Weise, N. Ukrainzcyk, M. Muthu, S. Lackner, E.A. Koenders, Interaction of wastewater microorganisms with geopolymer and cementitious materials, in: Proc. Microorg. Mater. Interact., RILEM, Toulouse, 2018, pp. 163–172.
[40] P. Lanari, A. Vho, T. Bovay, L. Airaghi, S. Centrella, Quantitative compositional mapping of mineral phases by electron probe micro-analyser, Geol. Soc. Spec. Publ. 478 (2019) 39–63, https://doi.org/10.1144/SP478.4.
[41] H. Riesemeier, K. Ecker, W. Görner, B.R. Müller, M. Radtke, M. Krumrey, Layout and first XRF applications of the BAMline at BESSY II, X-Ray Spectrom. 34 (2005) 160–163, https://doi.org/10.1002/xrs.750.
[42] B. Ravel, M. Newville, Athena, Artemis, Hephaestus: data analysis for X-ray absorption spectroscopy using IFEFFIT, J. Synchrotron Radiat. 12 (2005) 537–541, https://doi.org/10.1107/S0909049505012719.
[43] XAFS Spectra Library, (n.d.). http://cars.uchicago.edu/xaslib/search (accessed 1 Nov 2019).
[44] XAFS database, (n.d.). https://www.cat.hokudai.ac.jp/catdb/ (accessed 1 Nov 2019).
[45] D.A. McKeown, X-ray absorption spectroscopic study of copper in an amorphous copper silicate: chrysocolla, J. Non-Cryst. Solids 180 (1994) 1–10, https://doi.org/10.1016/0022-3093(94)90390-5.
[46] C.V. Chandran, T. Bräuniger, Efficient heteronuclear dipolar decoupling in solid-state NMR using frequency-swept SPINAL sequences, J. Magn. Reson. 200 (2009) 226–232, https://doi.org/10.1016/j.jmr.2009.07.006.
[47] M.D. Andersen, H.J. Jakobsen, J. Skibsted, Effects of T2-relaxation in MAS NMR spectra of the satellite transitions for quadrupolar nuclei: a ^{27}Al MAS and single-crystal NMR study of alum $KAl(SO_4)_2 \bullet 12H_2O$, J. Magn. Reson. 173 (2005) 209–217, https://doi.org/10.1016/j.jmr.2004.12.002.
[48] B.D.L. Parkhurst, C.A.J. Appelo, User's Guide to Phreeqc (Version 2)- a Computer Program for Speciation, and Inverse Geochemical Calculations, 1999.
[49] J. Horita, A. Ueda, K. Mizukami, I. Takatori, Automatic δD and $\delta^{18}O$ analyses of multi-water samples using H_2- and CO_2-water equilibration methods with a common equilibration set-up, Int. J. Radiat. Appl. Instrumentation. Part. 40 (1989) 801–805, https://doi.org/10.1016/0883-2889(89)90100-7.
[50] A.M. Harrisson, N.B. Winter, H.F.W. Taylor, X-ray microanalysis of microporous materials, J. Mater. Sci. Lett. 6 (1987) 1339–1340, https://doi.org/10.1007/BF01794611.
[51] O. Vogt, N. Ukrainczyk, C. Ballschmiede, E. Koenders, Reactivity and microstructure of metakaolin based geopolymers: effect of fly ash and liquid/solid contents, Materials (Basel). 12 (2019) 1–21, https://doi.org/10.3390/ma12213485.
[52] J.L. Provis, G.C. Lukey, J.S.J. Van Deventer, Do geopolymers actually contain nanocrystalline zeolites? A reexamination of existing results, Chem. Mater. 17 (2005) 3075–3085, https://doi.org/10.1021/cm050230i.
[53] M.H. Groothaert, J.A. Van Bokhoven, A.A. Battiston, B.M. Weckhuysen, R. A. Schoonheydt, Bis(μ-oxo)dicopper in Cu-ZSM-5 and its role in the decomposition of NO: a combined in situ XAFS, UV-vis-near-IR, and kinetic study, J. Am. Chem. Soc. 125 (2003) 7629–7640, https://doi.org/10.1021/ja029684w.
[54] L. Dupont, E. Guillon, J. Bouanda, J. Dumonceau, M. Aplincourt, EXAFS and XANES studies of retention of copper and lead by a lignocellulosic biomaterial, Environ. Sci. Technol. 36 (2002) 5062–5066, https://doi.org/10.1021/es025764o.
[55] R.K. Eby, F.C. Hawthorne, Structural relations in copper oxysalt minerals. I. Structural hierarchy, Acta Crystallogr. Sect. B. 49 (1993) 28–56, https://doi.org/10.1107/S0108768192007274.

[56] H.R. Oswald, A. Reller, H.W. Schmalle, E. Dubler, Structure of copper(II) hydroxide, $Cu(OH)_2$, Acta Crystallogr. Sect. C Cryst. Struct. Commun. 46 (1990) 2279–2284, https://doi.org/10.1107/s0108270190006230.
[57] S. Åsbrink, L.J. Norrby, A refinement of the crystal structure of copper(II) oxide with a discussion of some exceptional e.s.d.'s, Acta Crystallogr. Sect. B Struct. Crystallogr. Cryst. Chem. 26 (1970) 8–15, https://doi.org/10.1107/s0567740870001838.
[58] F. Farges, K. Benzerara, G.E. Brown, Chrysocolla redefined as spertiniite, AIP Conf. Proc. 882 (2007) 223–225, https://doi.org/10.1063/1.2644481.
[59] H. Takeda, S. Hashimoto, S. Honda, Y. Iwamoto, The coloring of geopolymers by the addition of copper compounds, Ceram. Int. 40 (2014) 6503–6507, https://doi.org/10.1016/j.ceramint.2013.11.103.
[60] P. Duxson, J.L. Provis, G.C. Lukey, F. Separovic, J.S.J. Van Deventer, ^{29}Si NMR study of structural ordering in aluminosilicate geopolymer gels, Langmuir. 21 (2005) 3028–3036, https://doi.org/10.1021/la047336x.
[61] B. Walkley, R. San Nicolas, M.A. Sani, J.D. Gehman, J.S.J. Van Deventer, J. L. Provis, Phase evolution of Na_2O-Al_2O_3-SiO_2-H_2O gels in synthetic aluminosilicate binders, Dalton Trans. 45 (2016) 5521–5535, https://doi.org/10.1039/c5dt04878h.
[62] S. Greiser, G.J.G. Gluth, P. Sturm, C. Jäger, $^{29}Si\{^{27}Al\}$, $^{27}Al\{^{29}Si\}$ and $^{27}Al\{^{1}H\}$ double-resonance NMR spectroscopy study of cementitious sodium aluminosilicate gels (geopolymers) and gel-zeolite composites, RSC Adv. 8 (2018) 40164–40171, https://doi.org/10.1039/c8ra09246j.
[63] K.J.D. MacKenzie, M.E. Smith, Multinuclear Solid-State NMR of Inorganic Materials (Oxford), Pergamon, 2002.
[64] P. Duxson, G.C. Lukey, F. Separovic, J.S.J. Van Deventer, Effect of alkali cations on aluminum incorporation in geopolymeric gels, Ind. Eng. Chem. Res. 44 (2005) 832–839, https://doi.org/10.1021/ie0494216.
[65] S. Greiser, P. Sturm, G.J.G. Gluth, M. Hunger, C. Jäger, Differentiation of the solid-state NMR signals of gel, zeolite phases and water species in geopolymer-zeolite composites, Ceram. Int. 43 (2017) 2202–2208, https://doi.org/10.1016/j.ceramint.2016.11.004.
[66] D.L. Carroll, T.F. Kemp, T.J. Bastow, M.E. Smith, Solid-state NMR characterisation of the thermal transformation of a Hungarian white illite, Solid State Nucl. Magn. Reson. 28 (2005) 31–43, https://doi.org/10.1016/j.ssnmr.2005.04.001.
[67] I.S. Chuang, G.E. Maciel, A detailed model of local structure and silanol hydrogen bonding of silica gel surfaces, J. Phys. Chem. B 101 (1997) 3052–3064, https://doi.org/10.1021/jp9629046.
[68] J.M. Eiler, B. Bergquist, I. Bourg, P. Cartigny, J. Farquhar, A. Gagnon, W. Guo, I. Halevy, A. Hofmann, T.E. Larson, N. Levin, E.A. Schauble, D. Stolper, Frontiers of stable isotope geoscience, Chem. Geol. 372 (2014) 119–143, https://doi.org/10.1016/j.chemgeo.2014.02.006.
[69] R.L. Hartman, H.S. Fogler, The unique mechanism of analcime dissolution by hydrogen ion attack, Langmuir. 22 (2006) 11163–11170, https://doi.org/10.1021/la061576q.
[70] R.L. Hartman, H.S. Fogler, Understanding the dissolution of zeolites, Langmuir. 23 (2007) 5477–5484, https://doi.org/10.1021/la063699g.
[71] M. Dietzel, E. Usdowski, Depolymerization of soluble silicate in dilute aqueous solutions, Colloid Polym. Sci. 273 (1995) 590–597, https://doi.org/10.1007/BF00658690.
[72] M. Dietzel, Dissolution of silicates and the stability of polysilicic acid, Geochim. Cosmochim. Acta 64 (2000) 3275–3281, https://doi.org/10.1016/S0016-7037(00)00426-9.
[73] V.C. Farmer, D.G. Lumsdon, An assessment of complex formation between aluminium and silicic acid in acidic solutions, Geochim. Cosmochim. Acta 58 (1994) 3331–3334, https://doi.org/10.1016/0016-7037(94)90088-4.
[74] H. Wonisch, F. Gérard, M. Dietzel, J. Jaffrain, O. Nestroy, J.P. Boudot, Occurrence of polymerized silicic acid and aluminum species in two forest soil solutions with different acidity, Geoderma. 144 (2008) 435–445, https://doi.org/10.1016/j.geoderma.2007.11.022.
[75] L.A. Hardie, The gypsum-anhydrite equilibrium at one atmosphere pressure, Am. Mineral. 52 (1967).
[76] R.L. Frost, Y. Xi, Is chrysocolla $(Cu,Al)_2H_2Si_2O_5(OH)_4{\cdot}nH_2O$ related to spertiniite $Cu(OH)_2$ - a vibrational spectroscopic study, Vib. Spectrosc. 64 (2013) 33–38, https://doi.org/10.1016/j.vibspec.2012.10.001.
[77] R.L. Frost, Y. Xi, B.J. Wood, Thermogravimetric analysis, PXRD, EDX and XPS study of chrysocolla $(Cu,Al)_2H_2Si_2O_5(OH)_4{\cdot}nH_2O$-structural implications, Thermochim. Acta 545 (2012) 157–162, https://doi.org/10.1016/j.tca.2012.07.011.